Energy & Environmental Science

ROYAL SOCIETY OF CHEMISTRY

REVIEW

View Article Online
View Journal | View Issue

Cite this: *Energy Environ. Sci.*, 2023, **16**, 5633

Powering the hydrogen future: current status and challenges of anion exchange membrane fuel cells

Jonghyun Hyun[a] and Hee-Tak Kim *[ab]

Received 1st June 2023,
Accepted 5th September 2023

DOI: 10.1039/d3ee01768k

rsc.li/ees

Hydrogen energy and related technologies are essential for combating climate change and meeting the growing energy demands. Despite being considered a key technology, proton exchange membrane fuel cells (PEMFCs) are yet to overcome their dependence on noble-metal catalysts, hindering progress toward a hydrogen economy. Recently, anion exchange membrane fuel cells (AEMFCs) have emerged as promising alternatives to PEMFCs owing to the use of inexpensive metals for both the catalysts and bipolar plates in alkaline environments. Although the AEMFC technology has achieved tremendous progress in materials development, several chronic problems need to be addressed. This review presents a comprehensive overview of the critical issues in the development of AEMFCs and the previous efforts made to resolve them. In addition, a comparative analysis between PEMFCs and AEMFCs is performed to diagnose the current status of AEMFCs from a practical perspective and to propose potential avenues for future development.

Broader context

Hydrogen, as a clean energy vector, has become increasingly crucial in combating climate change. In the hydrogen value chain, fuel cells play a vital role in harnessing hydrogen and converting chemical energy into electricity, which can be used in various industries, including transportation, industrial, and power generation. Although proton exchange membrane fuel cells (PEMFCs) have been the most studied type of fuel cell, anion exchange membrane fuel cells (AEMFCs) have recently gained attention due to their use of inexpensive materials. The recent remarkable developments in anion exchange membranes (AEMs) and ionomers (AEIs) have significantly improved the performance and durability of AEMFCs, shedding light on the path forward. However, the current status falls short of practical applicability, demanding a significant leap beyond the current level. In this article, we present a comprehensive review of AEMFCs, comparing them with PEMFCs using objective indicators. We summarize the problems associated with AEMFCs from a material and system perspective and suggest improvements accordingly. This review will provide insights for researchers and contribute to the progress of AEMFCs.

1. Introduction

Hydrogen is the most desired ecofriendly energy vector for preventing climate change and meeting the rising global energy demand. Fuel cells are electrochemical devices that can convert the chemical energy of hydrogen to electricity and are regarded as key enablers of hydrogen technologies. Among the many types of fuel cells, proton exchange membrane fuel cells (PEMFCs) are the most widely used, as exemplified by stationary fuel cells (FCgen® and FCwave® from Ballard™) and fuel cell electric vehicles (Nexo from Hyundai and Mirai from Toyota), because of their superior power performance and acceptable durability. PEMFC technology is grounded on fast oxygen reduction and hydrogen oxidation reactions catalyzed by noble-metal catalysts, such as platinum (Pt) coupled with a proton exchange membrane (PEM). However, in terms of commercialization, PEMFC technology still suffers from high system costs.[1,2] There are many reasons for this limitation, but the Achilles' heel for such a price increase is the acidic environment in PEMFCs due to the use of proton exchange membranes and ionomers. In general, an acidic environment is corrosive to materials, thereby compelling the use of noble-metal catalysts and perfluorinated ionomers that are stable under acidic conditions as well as acid-resistant bipolar plates.

Anion exchange membrane fuel cells (AEMFCs) have recently emerged as cost-effective alternatives to PEMFCs. AEMFCs are a type of fuel cell that use anion exchange membranes (AEMs) as

[a] *Department of Chemical and Biomolecular Engineering, Korea Advanced Institute of Science and Technology (KAIST), Daejeon 34141, Republic of Korea. E-mail: heetak.kim@kaist.ac.kr*
[b] *Advanced Battery Center, KAIST Institute for the NanoCentury, Korea Advanced Institute of Science and Technology (KAIST), 335 Gwahangno, Yuseong-gu, Daejeon 34141, Republic of Korea*

electrolytes to facilitate the migration of hydroxide ions (OH^-). This technology originates from the alkaline fuel cell, which was first developed in the 1960s in response to NASA's Gemini, Apollo, and Space Shuttle projects.[3] The alkaline fuel cell technology that utilizes highly concentrated alkaline solution as an electrolyte has evolved into AEMFC technology by replacing the liquid electrolyte with an AEM. However, it was not until the early 2000s that the technology started gaining significant attention as a potential alternative to PEMFCs. Since the early 2000s, there have been significant research and development efforts into AEMFCs, with numerous academic and industrial groups working to improve the efficiency and durability of this technology. There have been several demonstration projects and research consortia focused on AEMFCs in recent years. AEMFCs offer several advantages over other types of fuel cells, including their ability to use non-precious metal (NPM) catalysts, hydrocarbon membranes, and cheap metal bipolar plates, which significantly reduce the cost of the fuel cells.

AEMFCs constitute a relatively new technology that is currently under development. As with any new field, several critical challenges have been faced and overcome. One of the most significant challenges to date has been the achievement of anion exchange membrane stability under highly alkaline conditions.[4,5] Researchers in this field have been working hard to overcome these challenges, and significant progress has been made in recent years. Based on these efforts, state-of-the-art AEMFCs can now deliver remarkable power performances that surpass those of ordinary PEMFCs with durability of over 2000 h.[6] Several manufacturers (AFC Energy and HydroLite) are now working on commercializing AEMFCs for use in stationary power generation and other applications. However, practical applications of AEMFCs still remain challenging owing to various instabilities and degradation modes that are not yet clearly identified and understood, in addition to a myriad of requirements for optimizing fuel cell systems for specific applications. Similar to other types of fuel cells, the development of electrochemically active and durable catalysts is indispensable for commercialization. Furthermore, there is a high demand for precise water and thermal management to maintain optimal operating conditions.[7,8]

The present review provides an overview of AEMFC technology, covering its key features such as structures, materials, and cost-effectiveness, as well as a comparative analysis with PEMFCs to assess the current status, strengths, and weaknesses. We then delve into the critical issues concerning AEMFCs, including their power performance and durability, and provide detailed and organized accounts of their causes, such as membrane degradation, catalyst activity and stability, and water management challenges. We also highlight the practical challenges presented by these issues and discuss their implications for future developments in AEMFC technologies. Furthermore, we identify unexplored areas within this technology sector and suggest some research directions and solutions for practical development of AEMFCs. It is expected that a timely review could stimulate more researchers to develop the technology and provide the necessary impetus for future progress.

2. Key features of AEMFCs and drivers of AEMFC development

The structure of AEMFCs, as shown in Fig. 1a, is similar to that of PEMFCs. Both types of fuel cells have a membrane electrode assembly (MEA) as their key component. The MEA consists of a membrane and a pair of catalyst layers (CLs) and diffusion layers within a single cell. The single-cell structure is repeated in a stack, like in the PEMFCs, to deliver high power and a high working voltage. However, the materials used for the AEMFC MEA are different because the operating environment of the AEMFC is alkaline, contrary to the acidic environment of the PEMFC, which offers the possibility of reducing the fuel cell cost. NPM-based oxygen reduction reaction (ORR) catalysts are used in AEMFCs, which is in contrast to the dominantly used Pt-based catalysts in PEMFCs. Protons and hydroxide ions

Jonghyun Hyun

Jonghyun Hyun joined the Korea Advanced Institute of Science and Technology (KAIST) in 2014 to pursue both his bachelor's and master's degrees in chemical and biomolecular engineering. Currently, he is engaged in his PhD research, under the guidance of Professor Hee-Tak Kim. His primary research expertise lies in AEM fuel cells and AEM water electrolysis, focusing on enhancing performance and durability through a comprehensive understanding of interfacial phenomena between catalysts and ionomers. Additionally, he is dedicated to optimizing the design of catalyst layers and MEAs to achieve further advancements in these technologies.

Hee-Tak Kim

Professor Hee-Tak Kim is a full professor at the Department of Chemical Engineering and serves as the head of the advanced battery center and the Frontier Research Lab at KAIST. His primary research expertise lies in the design of electrochemical energy devices, which encompass fuel cells, water electrolysis and secondary batteries. Through the integration of electrochemical engineering, materials engineering, and interfacial engineering, his research group delves into innovative concepts and efficient designs aimed at addressing crucial challenges within this domain.

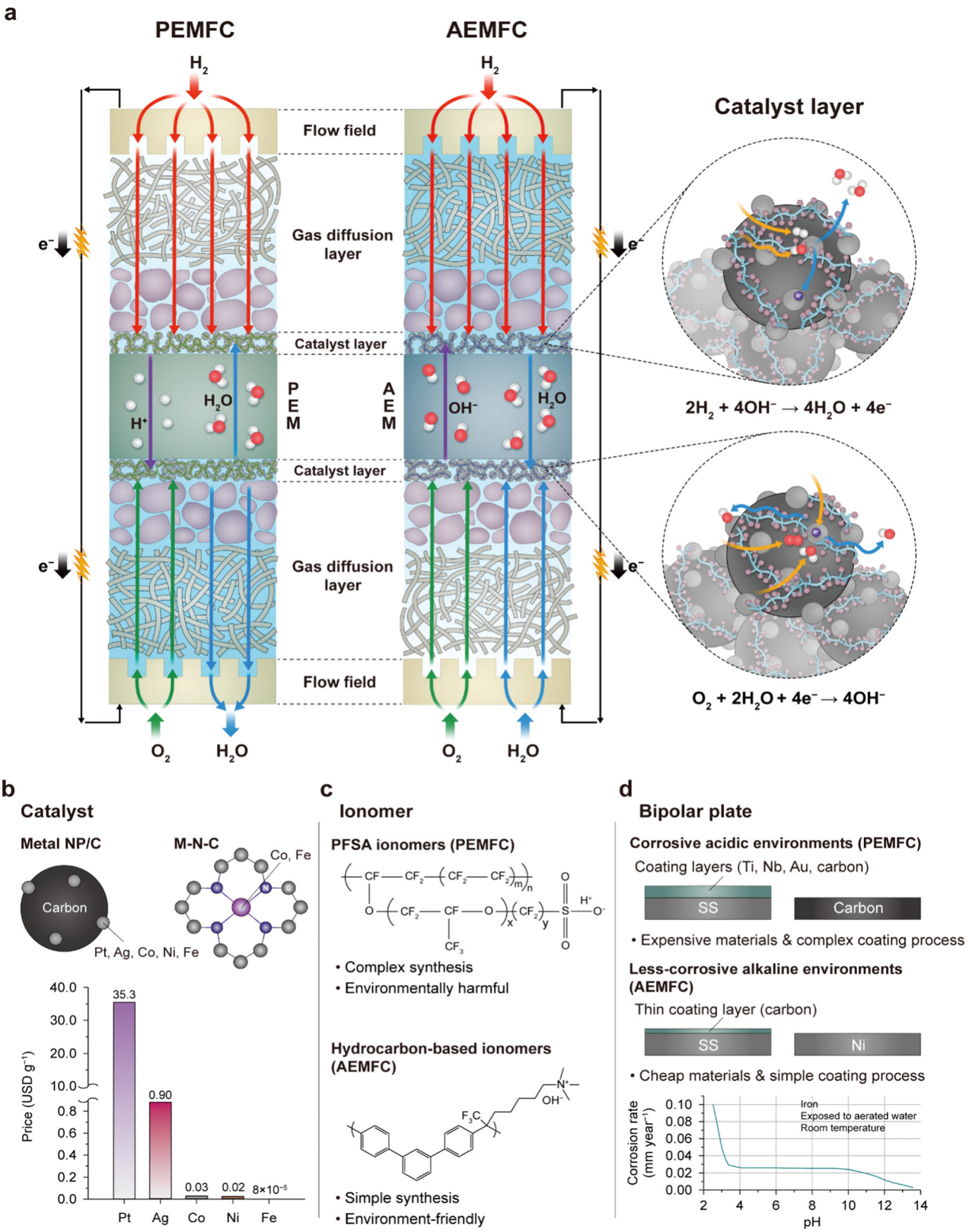

Fig. 1 Potential cost-reduction with AEMFCs. (a) Schematic illustrations of the structures and electrochemical reactions of PEMFCs and AEMFCs. Three reasons for cost savings *via* switching from PEMFCs to AEMFCs: (b) catalyst, (c) ionomer, and (d) bipolar plate. The metal prices in (b) were calculated by referring to the London Metal Exchange.[9] The corrosion rate of iron with pH is reprinted from ref. 10.

migrate in opposite directions in PEMFCs and AEMFCs, respectively, resulting in different electro-osmosis behaviors. In AEMFCs, water is consumed at the cathode, unlike water generation at the cathode in PEMFCs, leading to different water distributions in the MEAs and thereby requiring different water management strategies.

Various factors contribute to the cost-effectiveness of AEMFCs. One such factor is the use of less-corrosive NPMs, which are expected to have high catalytic activities owing to the alkaline environment. Carbon-supported metal nanoparticles and N-coordinated metal catalysts are being studied parallelly as catalysts (Fig. 1b). Regarding the former, carbon modification technologies such as the fluorination of the carbon support surface[11] attract interest because of their critical role in minimizing water flooding on the anode side of AEMFCs. While Pt is mainly being used at the single-cell level, Ag,[12,13] Co,[14] Ni,[15] and Fe metals[16] or alloys[17,18] have been studied as catalysts for AEMFCs. Indeed, the prices of NPMs are 2–5 orders of magnitude lower than that of Pt, as demonstrated in the price comparison plot in Fig. 1b. This has the potential to significantly reduce the cost of fuel cells.

The second aspect of cost savings is the utilization of hydrocarbon-based ionomers (Fig. 1c). Under acidic conditions, hydrocarbon-based PEMs are easily degraded primarily through hydrolytic reactions;[19,20] they degrade much faster in Fenton's reagent than perfluorosulfonic acid (PFSA) membranes.[21,22] Moreover, their insufficient mechanical stabilities under repeated exposure to humid and dry conditions make them unsuitable for dynamic PEMFC operations.[23] Therefore, the industry has standardized the use of PFSA membranes to ensure durability of PEMFCs. However, in alkaline environments, the degradation of hydrocarbon ionomers can be mitigated.[4] Indeed, state-of-the-art hydrocarbon AEMs and ionomers (AEIs) have demonstrated long-term operations in AEMFCs.[6,24,25] Compared to the complex and harmful synthesis process of the PFSA ionomer, the synthesis of hydrocarbon ionomers is generally simpler and milder, which makes them more cost-effective.[5,26] Although the fluorinated backbone of the PFSA ionomer provides high chemical stability that is sufficient for operations exceeding 10 000 h, it takes a long time to biodegrade, requiring expensive postprocessing after use. For reference, fluorinated polyacrylates, another type of fluorinated polymer, have an estimated biodegradation half-life of approximately 1200–1700 years.[27,28] In contrast, the biodegradability of hydrocarbon ionomers is relatively faster, which makes them a more ecofriendly option.

One additional driver of cost reduction is the use of low-cost metal bipolar plates, including those made of materials like stainless steel or nickel. This is in contrast to the use of thick acid-resistant surface-coated metals or highly graphitic carbon bipolar plates in PEMFCs owing to the corrosive nature of the Nafion ionomer. As seen in Fig. 1d, the corrosion rate of iron reduces as the pH increases, indicating the possibility of using inexpensive stainless steel as the bipolar plate in AEMFCs. The commercial carbon-coated stainless steel 316L has been shown to maintain a low internal contact resistance (<20 mΩ cm^2) in the AEMFC environment,[29] but an additional coating process is necessary in PEMFCs as their internal contact resistances exceed 200 mΩ cm^2 due to surface corrosion.[30,31]

3. Performance and durability of AEMFCs compared with PEMFCs

The foundation of fuel cell commercialization is based on achieving sufficient performance and durability. Previous papers document the performance, durability, and milestones for AEMFCs.[63–65] Although significant progress has been made in improving their performance and durability, there are still considerable gaps for meeting practical demands. For objective assessments of the current status of AEMFCs, their performance and durability are compared with those of state-of-the-art PEMFCs in Fig. 2.

Fig. 2a compares the specific peak power densities reported for Pt-based AEMFC and PEMFC single cells, which are obtained by dividing the peak power density by the amount of Pt catalyst used (Table 1). One notable feature here is that AEMFCs use significantly larger amounts of Pt (>0.3 mg$_{Pt}$ cm^{-2}) compared to PEMFCs (<0.3 mg$_{Pt}$ cm^{-2}). Furthermore, the specific peak power of AEMFCs is less than that of PEMFCs. The peak power density of AEMFCs is comparable to that of PEMFCs, which is attributed to the use of a larger amount of Pt catalyst. Considering the good ORR kinetics of Pt in the alkaline environment,[66,67] the relatively low specific peak power of the AEMFC suggests low Pt utilization. This motivates further research on the CL structure, water management, CO_2 poisoning, and catalyst/AEI interface with the aim of augmenting Pt utilization.

Fig. 2b shows the peak power densities of NPM catalysts (metal nanoparticles supported on carbon (metal NP/C) and Fe–N–C) at the PEMFC and AEMFC cathodes reported over the past 6 years (Table 2). Despite being in the early stages of research, a few AEMFCs based on NPM catalysts have exhibited a notable power performance of over 1.5 W cm^{-2}, which is far higher than that of PEMFCs.[13,16] Remarkably, a Fe–N–C catalyst-based AEMFC was reported with a power density of over 2.0 W cm^{-2} and durability of more than 150 h,[16] demonstrating the potential for cost-effective AEMFC development and stimulating further research. However, the use of pure O_2, excessive supply of reaction gases, and high catalyst loading are still challenges for NPM-based AEMFCs. Due to the low activity site density of NPM catalysts, large amounts of the catalysts are required, leading to thick CLs and making optimal design difficult for both PEMFCs and AEMFCs.

Durability is a crucial factor for practical applications of fuel cells. However, until recently, the alkaline stabilities of AEMs and AEIs were too low to enable long-term operation. The discovery of the ether-cleavage degradation pathway and subsequent development of ether-free ionomers have achieved significant strides in improving the alkaline stabilities of AEMs and AEIs. However, the durability of AEMFCs is still lacking, as evidenced by the comparison of the lifetimes of AEMFCs and PEMFCs under constant current operation, as published recently (Fig. 2c and Table 3). While PEMFCs have various durability evaluation protocols tailored to their specific purposes, AEMFCs do not have a standardized protocol and are typically evaluated through constant current operation.

Several PEMFCs exhibit durabilities of 10 000 h or more, exceeding the 2030 DOE target for high-performance vehicles

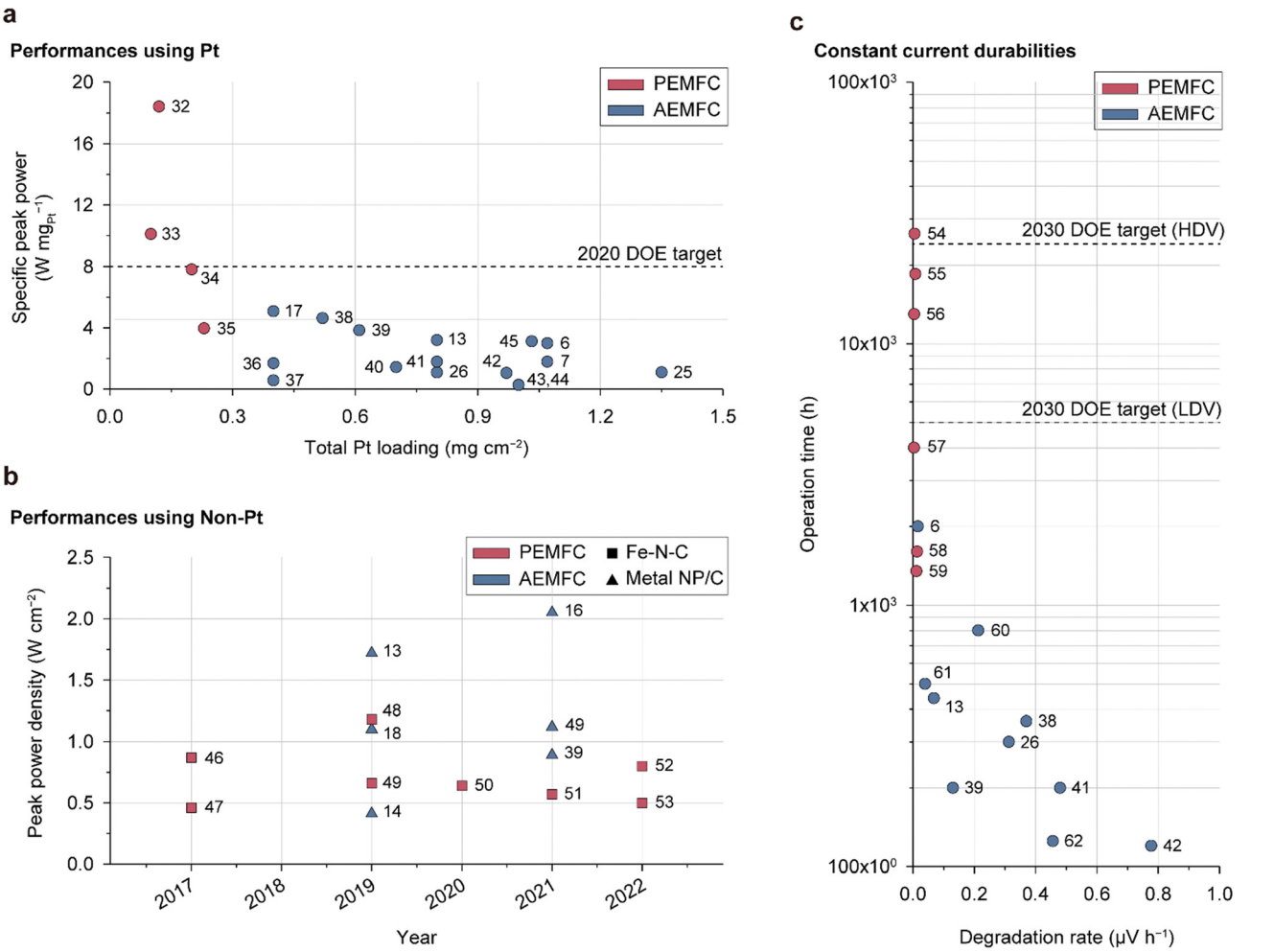

Fig. 2 Performance and durability comparisons of state-of-the-art PEMFCs and AEMFCs. (a) Specific peak power density *versus* total Pt loading for fuel cells containing Pt-based cathodes: peak power density is standardized by the total Pt loading in both electrodes (Table 1).[6,7,13,17,25,26,32–45] (b) Peak power densities of fuel cells containing non-Pt catalyst-based cathodes over the past 6 years (Table 2).[13,14,16,18,39,46–53] (c) Fuel cell operation time *versus* degradation rate: the fuel cells are operated under the constant current mode (Table 3).[6,13,26,38,39,41,42,54–62]

(HDVs),[68] while the longest lifespan of any reported AEMFC to the best of our knowledge has been 2000 h.[6] Despite the good stabilities of metal catalysts under alkaline conditions and recent developments in alkali-stable AEMs and AEIs, present AEMFCs do not meet the target durability level, highlighting the need for intensive research directed at enhancing durability. The reasons for the rapid degradation of AEMFCs are described and discussed in Section 5.

4. Challenges and solutions for improving the power performance of AEMFCs

Power performance is an essential characteristic of a fuel cell as it is closely linked to its energy conversion efficiency and stack/system size. It is typically evaluated using a polarization curve that provides information on various polarization components. The dependency on operating conditions is the basis of an optimal fuel cell system design, considering heat management and the balance of the plant. Regarding the power performances of AEMFCs, most studies have focused on MEA development, while very little attention has been devoted to stack- or system-level designs. In the pursuit of enhancing the power performance of the MEA, key materials such as AEMs, AEIs, and catalysts have been studied extensively. However, the CLs and interfaces are less explored despite their strong impact on the power performance. Moreover, only a few studies have reported quantitative analyses of the polarization curve; therefore, the factors affecting the power performance have not been understood fully.

The power performance of AEMFCs is largely dictated by the properties of the catalyst, AEM, AEI, and gas-diffusion layer. Fast ORR/hydrogen oxidation reaction (HOR) kinetics of catalysts and high OH^- conductivity of the AEM/AEI materials can ensure higher power performance under the given operating conditions. Moreover, the composition and structure of the CL are of great importance for enhancing the power performance since the electrochemical reactions in AEMFCs occur at triple-phase boundaries (TPBs) at which the gas feed, catalyst, and

Table 1 List of power performances for typical PEMFCs and AEMFCs based on the Pt-based cathode corresponding to data in Fig. 2a

Fuel cell type	Pt loading (anode/cathode, mg_{Pt} cm^{-2})	Peak power density (W cm^{-2})	Operating conditions[a]	Ref.
PEMFC	0.05/0.07	2.21	80 °C, 100% RH, H_2/O_2, 150 kPa_{abs}	32
	0.01/0.09	1.01	80 °C, 100% RH, H_2/O_2, 150 kPa_{abs}	33
	0.1/0.1	1.56	80 °C, 100% RH, H_2/O_2, 150 kPa_{abs}	34
	0.1/0.13	0.909	80 °C, 100% RH, H_2/O_2, 150 kPa_{abs}	35
AEMFC	0/0.4	2.03	95 °C, 88/97 °C, H_2/O_2, 250 kPa	17
	0.26/0.26	2.4	80 °C, 75%/100% RH, H_2/O_2, 1.3 bar	38
	0.28/0.33	2.34	80 °C, 75%/100% RH, H_2/O_2, 1.3 bar	39
	0.4/0.4	2.55	80 °C, 92% RH, H_2/O_2	13
	0.448/0.672	3.21	80 °C, 70/74 °C, H_2/O_2	45
	0.467/0.6	3.2	80 °C, 72/74 °C, H_2/O_2	6
	0.473/0.6	1.9	60 °C, 45/46 °C, H_2/O_2	7
	0.4/0.4	1.42	60 °C, 56/58 °C, H_2/O_2	41
	0.2/0.2	0.67	80 °C, 100% RH, H_2/O_2	36
	0.1/0.6	1.0	80 °C, 100% RH, H_2/O_2, 285 kPa	40
	0.4/0.4	0.86	95 °C, 95/97 °C, H_2/O_2, 0.1 MPa_g	26
	0.5/0.6	1.26	80 °C, 100%/50% RH, H_2/O_2, 147.5 kPa	25
	0.4/0.0026	0.224	40 °C, 80% RH, H_2/O_2	37
	0.47/0.5	1.01	60 °C, 51/56 °C, H_2/O_2, 0.1 MPa at the anode	42
	0.5/0.5	0.261	60 °C, 100% RH, H_2/O_2	43
	0.5/0.5	0.25	60 °C, 100% RH, H_2/O_2	44

[a] Cell temperature, humidity conditions (anode/cathode), reaction gas, and back-pressure are presented in order.

Table 2 List of power performances for typical PEMFCs and AEMFCs based on the non-Pt-based cathode corresponding to data in Fig. 2b

Fuel cell type	Catalyst type	Peak power density (W cm^{-2})	Operating conditions[a]	Ref.
PEMFC	FeNC	0.87	80 °C, 100% RH, H_2/O_2, 1/2 bar	46
	FeNC	0.46	80 °C, H_2/O_2, 1 bar	47
	FeNC	1.18	80 °C, 100% RH, H_2/O_2, 2.5 bar	48
	FeNC	0.66	80 °C, 100% RH, H_2/O_2, 1 bar	49
	CoNC	0.64	80 °C, 100% RH, H_2/O_2, 1 bar	50
	FeNC	0.57	80 °C, 100% RH, H_2/O_2, 1 bar	51
	FeNC	0.8	80 °C, 100% RH, H_2/O_2, 1 bar	52
AEMFC	Ag/C	1.72	80 °C, 92% RH, H_2/O_2	13
	Mn-Co/C	1.1	60 °C, 100% RH, H_2/O_2, 0.1 MPa	18
	Co/C	0.412	60 °C, 100% RH, H_2/O_2	14
	FeNC	2.05	80 °C, 70/75 °C, H_2/O_2, 200 kPa	16
	FeNC	1.12	60 °C, H_2/O_2, 1 bar	53
	Co/C	0.891	80 °C, H_2/O_2, 0.5 bar	39

[a] Cell temperature, humidity conditions (anode/cathode), reaction gas, and back-pressure are presented in order.

ionomer coexist. Furthermore, several chronic problems, such as strong ionomer adsorption on the catalyst surface, severe water imbalance between the two electrodes, and formation of carbonate species by CO_2, are crucial to the power performance of AEMFCs.

In this section, we review the challenges related to enhancing the power performance and the approaches to address them. We first focus on the issues concerning materials and then cover some issues pertaining to power performance, such as water flooding and CO_2 poisoning. To explain the drawbacks from a practical perspective, the current status of ionomer and catalyst developments for AEMFCs is compared with those of PEMFCs. The efforts regarding MEA design for power performance enhancement are also summarized.

4.1. Material development

4.1.1. AEMs. Over the last decade, AEMs are the most extensively studied components in AEMFC technology, and their significant progress has enabled the development of high-performing AEMFCs. In the early stages of AEM development, the major challenge was overcoming low ionic conductivity. For example, the fluoropoly(olefin) membrane exhibited a low ionic conductivity of 70 mS cm^{-1} at 80 °C even when submerged in water owing to the low mobility of OH^- and low dissociation of the trimethyl amine (TMA) hydroxide moiety.[42] This mobility (21.6×10^{-8} m^2 s^{-1} V^{-1}) is only half of that of H^+ in Nafion (36.2×10^{-8} m^2 s^{-1} V^{-1}),[81] and the pK_b value of TMA hydroxide (4.2) is much lower than the $-pK_a$ value of the sulfonic acid group (6.0). Various efforts have been made to achieve high ionic conductivity, including screening different types of backbones[24,82] and cationic groups,[83] introducing alkyl spacers or extenders,[84–86] adopting multicationic groups,[87] and using composite membranes with ion-conductive additives.[88] Because of these efforts, the ionic conductivities of state-of-the-art AEMs are now approaching those of cation exchange membranes (CEMs) under high humidity or in a swollen state with liquid water (Fig. 3a and Table 4). Recent reviews offer systematic descriptions of the evolutionary processes and structural designs of AEMs.[89–91] To avoid redundancy, we focus on four specific AEMs that demonstrate exceptionally high ionic conductivities.

Fig. 3b and Table 5 provide information on the structures, types of backbones, types of cationic groups, and ion exchange capacities (IECs) of the four highly conductive AEMs (polyethylene with hexyl TMA side groups, polynorbornene with hexyl TMA side groups, polyphenylene with piperidinium side groups, and poly(fluorene-*co*-phenylene) with piperidinium side groups). The ionic conductivity of each AEM is indicated in Fig. 3a. The polyethylene-based polymer (1), developed by Varcoe's group, stands as one of the pioneering materials for highly conductive

Table 3 List of durability values of typical PEMFCs and PEMFCs corresponding to data in Fig. 2c

Fuel-cell type	Operation time (h)	Degradation rate (μV^{-1})	Operating conditions[a]	Ref.
PEMFC	26 300	0.005	0.8 A cm^{-2}, 70 °C, 100% RH, H_2/air	54
	18 500	0.0075	0.29 A cm^{-2}, 71–72 °C, 100% RH, H_2/air	55
	12 860	0.0035	0.26 A cm^{-2}, 60–65 °C, 0%/60–75% RH, H_2/air	56
	4000	0.0031	0.4 A cm^{-2}, 60 °C, 100% RH, H_2 + CO_2/air	57
	1600	0.0133	0.25 A cm^{-2}, 200 °C, H_2 + CO_2 + CO + N_2/air	58
	1350	0.011	0.4 A cm^{-2}, 80 °C, 100% RH, H_2/air	59
AEMFC	2000	0.0154	0.6 A cm^{-2}, 75 °C, 72/74 °C, H_2/O_2	6
	800	0.2125	0.2 A cm^{-2}, 80 °C, 100% RH, H_2/O_2	60
	500	0.0393	0.5 A cm^{-2}, 120 °C, 40% RH, H_2/O_2	61
	440	0.068	0.6 A cm^{-2}, 70 °C, 92% RH, H_2/air (CO_2 free)	13
	360	0.37	0.6 A cm^{-2}, 70 °C, 68.5/72 °C, H_2/O_2	38
	300	0.3128	0.5 A cm^{-2}, 95 °C, 94/95 °C, H_2/air (CO_2 free)	26
	200	0.13	0.2 A cm^{-2}, 70 °C, 90%/100% RH, H_2/O_2	39
	200	0.48	0.3 A cm^{-2}, 70 °C, 68/70 °C, H_2/O_2	41
	125	0.456	0.2 A cm^{-2}, 80 °C, 100% RH, H_2/air (CO_2 free)	62
	120	0.7776	0.6 A cm^{-2}, 60 °C, H_2/O_2	42

[a] Current density, cell temperature, humidity conditions (anode/cathode), and reaction gas are presented in order.

AEMs.[12] The AEMFC utilizing this polyethylene-based polymer exhibited an impressive power density of 2.55 W cm^{-2} with a Pt/C cathode and a notable 1.72 W cm^{-2} with an Ag/C cathode. Moreover, when driven at 0.6 A cm^{-2} for 440 h, the AEMFC demonstrated a mere 7% voltage loss, showcasing its exceptional durability. Ongoing research on polyethylene-based AEMs[92–94] continues to inspire numerous subsequent developments in the field. The polynorbornene polymer (2) features a remarkably high IEC (3.59), which accounts for its high conductivity. Normally, an increase in the IEC leads to excessive water swelling, resulting in reduced mechanical stability. To address this issue, the polynorbornene AEM is partially cross-linked by linking the side groups, thereby controlling its swelling behavior. This AEM was first reported by Huang *et al.*[95] and has been the subject of numerous studies by various researchers.[24,72,96] The AEMFC using the polynorbornene-based AEM exhibits the highest power density (3.5 W cm^{-2}) achieved to date[97] and exceptionally high durability (2000 h).[6] The superior power performance is attributed not only to its high ionic conductivity but also to its fast water transport properties; the water generated at the anode readily moves to the cathode through the AEM, achieving a well-balanced water distribution inside the MEA. This prevents drying of the cathode even at remarkably high current densities ($\sim$10 A cm^{-2}). The polyphenylene with piperidinium side groups (3), which was first reported by Yan's group, also has a high IEC (2.37) and low water swelling ratio ($<$20%).[26] The low water swelling ratio is attributed to its rigid and hydrophobic polyphenylene backbone structure and high molecular weight. A single cell employing the polyphenylene AEM maintains a hydrogen gas cross-over of less than 10 sccm even after 5000 wet/dry cycles, demonstrating its high mechanical strength. Lee's group synthesized poly(fluorene-*co*-phenylene) with piperidinium side groups (4)[39] and fabricated its reinforced membrane with a porous polyethylene support.[38] The reinforced membrane exhibited a significant reduction in water uptake and swelling ratio as well as improved mechanical strength, leading to an impressive durability of over 300 h and a low voltage degradation rate (0.37 mV h^{-1}). Furthermore, the copolymer was found to be a promising candidate for use as an AEI binder because the polyfluorene segment mitigates strong absorption of the phenylene segment on the Pt surface, which causes a drastic decrease in HOR activity due to its nonrotatable properties. The AEMFC employing the copolymer as both AEM and AEI delivers a high power density of 2.4 W cm^{-2}.

Similar to conventional CEMs, the ionic conductivities of AEMs are impacted by the relative humidity (RH) since the level of dissociation of the cation–anion groups and mobility of OH^- increase with higher water content in the AEMs. Although the AEMs mentioned earlier demonstrate exceptional conductivities when fully hydrated, they have lower ion conductivities than CEMs at low RHs, as depicted in Fig. 3c. The significant decrease in ionic conductivity at low RHs for the AEMs compared to the perfluorinated CEMs can be attributed to the morphologies of the water channels inside the AEMs (Fig. 3d). With increasing RH, the hydrophilic domain of the CEM or AEM expands through hydration and becomes more connected to the nearby domains, eventually forming well-connected channels for proton transport at a certain RH known as the "percolation threshold." As observed for hydrocarbon-based CEMs,[98,99] ionomers with rigid backbones form narrower water channels of AEMs compared to perfluorinated CEMs, resulting in percolation thresholds at higher RH and a less-connected water channel structure (Fig. 3d). Although increasing the IEC can improve this issue, this approach is practically limited by the resulting decrease in mechanical properties.

Alignment of the water channel in the thickness direction can significantly improve the ionic conductivity at low RH.[100] This was recently achieved with an AEM having a polyvinyl backbone and ferrocenium cationic group, whose structure is shown in Fig. 3e (indicated by 5).[61] The AEM showed similar or even higher ionic conductivity than the CEM. The ferrocenium moiety aligns with the direction of the external magnetic field owing to its paramagnetic property, presenting a possibility for aligning the water channels in the thickness direction, which is the most preferred morphology for shortening the OH^-

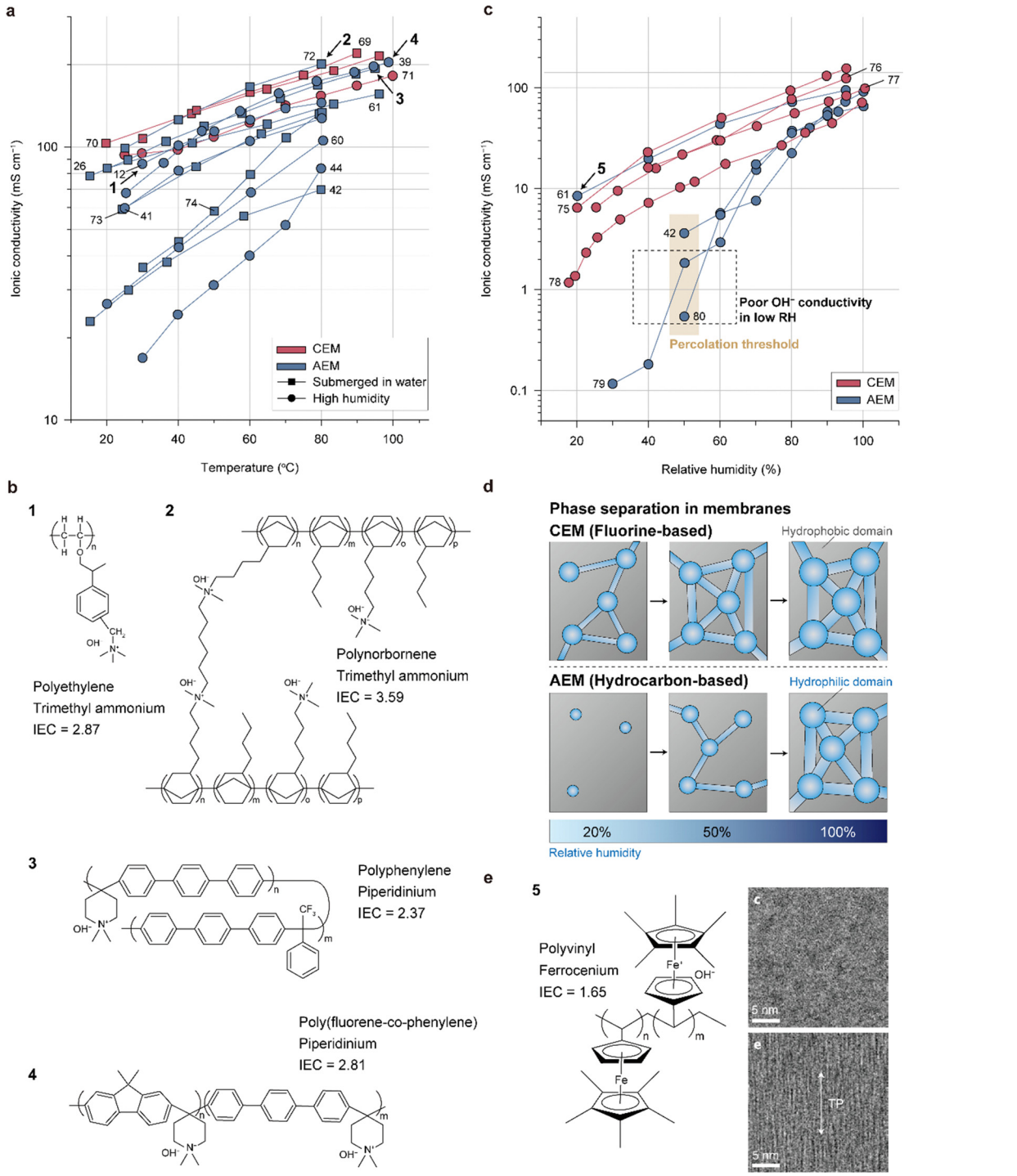

Fig. 3 Ionic conductivities and structures of the representative membranes. (a) Ionic conductivities of state-of-the-art CEMs and AEMs as functions of temperature measured under highly humid environments or in liquid water (Table 4).[12,26,39,41,42,44,60,61,69–74] (b) Chemical structures of representative AEMs with similar ionic conductivities as CEMs. (c) Ionic conductivities of state-of-the-art CEM and AEM as functions of the relative humidity (RH, Table 5).[42,61,75–80] (d) Schematic showing the evolution of the phase-separated morphology with increasing RH for the CEM and AEM. (e) Chemical structure of polyvinyl ferrocenium (left) and cross-sectional transmission electron microscopy (TEM) images of the polyvinyl ferrocenium membranes with unaligned (upper right) and aligned (lower right) structures in the through-plane direction. Cross-sectional TEM images are adapted with permission.[61] The membranes were stained with tungstate to clearly observe the phase-separation morphology. In the images, the dark and bright regions correspond to the hydrophilic and hydrophobic domains, respectively.

transport pathways. The phase-separation morphologies of the AEMs prepared with and without an external magnetic field are compared in Fig. 3e; the dark regions corresponding to the hydrophilic ferrocenium domains are aligned and connected in

Table 4 Chemical structures, IECs, and ionic conductivity measurement conditions for the membranes displayed in Fig. 3a

Membrane type	Chemical structure	IEC (meq g^{-1})	Conductivity measurement environment	Ref.
CEM	PFSA	—	Water	69
	Ferrocyanide-coordinated polymer/phosphotungstic acid	1.48		70
	PFSA/sulfonated CNT	0.95	High humidity	71
AEM	Poly(norbornene) with TMA	3.59	Water	72
	Poly(aryl piperidinium)	2.37		26
	Poly(vinylferrocene)	1.65		61
	Poly(arylene piperidinium)	2.34		73
	Fluoropoly(olefin) with TMA	1.12		42
	Partial diallyl bisphenol A poly(arylene ether) with TMA	2.16		74
	Poly(arylimidazoliums)	2.86	95% RH	44
	Low-density polyethylene with TMA	2.87		12
	Poly(arylene ether sulfone) with imidazolium	2.2	100% RH	60
	Polyphenylene/polysulfone with TMA	2.3		41
	Poly(fluorenyl aryl piperidinium)	2.81		39

Table 5 Chemical structures, IECs, and ionic conductivity measurement temperatures for the membranes displayed in Fig. 3c

Membrane type	Chemical structure	IEC (meq g^{-1})	Conductivity measurement temperature	Ref.
CEM	Polyphenylene with sulfonate	2.4	80 °C	75
	PFSA/reduced graphene oxide	1.5		76
	PFSA/reduced graphene oxide	0.84		77
	PFSA	0.93		78
AEM	Cu^{2+}-cross-linked chitosan	1.6	25 °C	79
	Polyethylene glycol with imidazolium	1.96	80 °C	80
	Fluoropoly(olefin) with TMA	1.12		42
	Poly(vinylferrocene)	1.65		61

the through-plane direction. This result motivates future research for achieving high ionic conductivity under low RH conditions by aligning the water channels and achieving percolation at a much lower RH.

4.1.2. ORR catalysts. The higher ORR kinetics observed in alkaline electrolytes compared to acidic electrolytes is a major incentive for utilizing AEMFCs. Although the reason for this phenomenon is not fully understood, the outer-sphere electron transfer mechanism proposed by Ramaswamy and Mukerjee presents a feasible explanation (Fig. 4a and b).[67] They considered the electrical double-layer structure formed on the ORR electrode. During fuel cell operation, the cathode potential is higher than the potential of zero charge (PZC), resulting in a positively charged cathode surface and a negatively charged double layer. In both acidic and alkaline electrolytes, the inner Helmholtz plane (IHP) consists of three molecules (H_2O, OH^-, and O_2), with the oxygen atoms in these molecules oriented toward the electrode surface due to the orientations of their dipoles under an electric field. At the outer Helmholtz planes (OHPs) in acidic electrolytes, hydrated H^+, hydrated O_2, and hydrated anions are present, while alkaline electrolytes contain hydrated O_2 and hydrated cations. The ORR mechanism based on the double-layer structure is provided in Fig. 4c. In an acidic electrolyte, the ORR involves electron transfer from the electrode to the chemisorbed O_2 molecule, which is the rate-determining step (RDS), followed by proton transport from the OHP to IHP. All these reactions are part of the inner-sphere

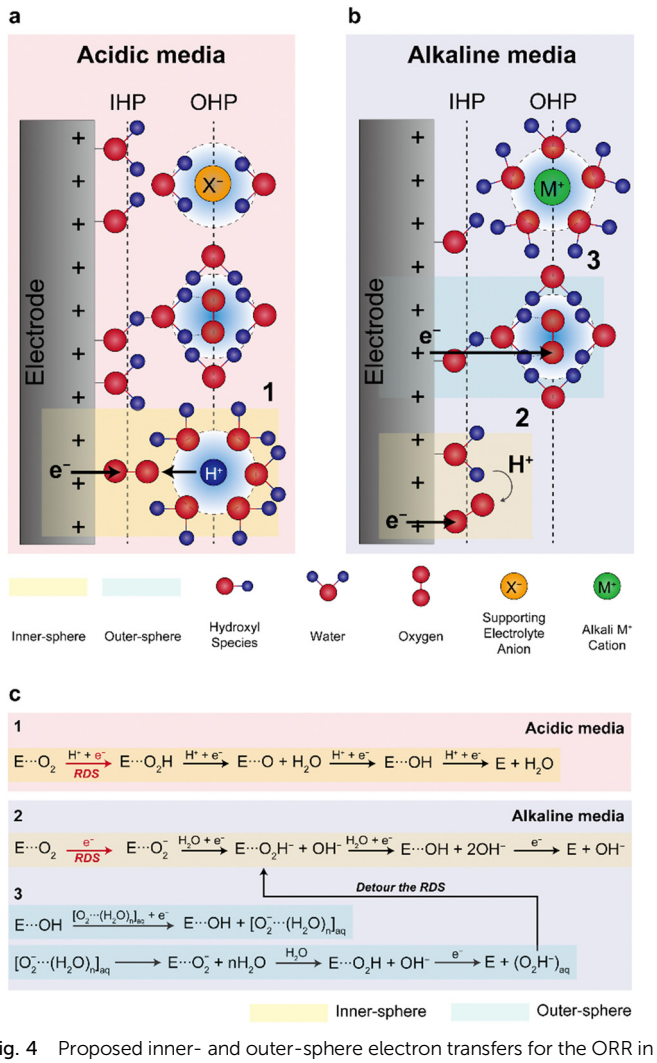

Fig. 4 Proposed inner- and outer-sphere electron transfers for the ORR in alkaline media. Schematic illustrations of the double-layer structures in (a) acidic and (b) alkaline media during the ORR and (c) reaction mechanisms in the acidic and alkaline media. (a) and (b) are adapted with permission.[67]

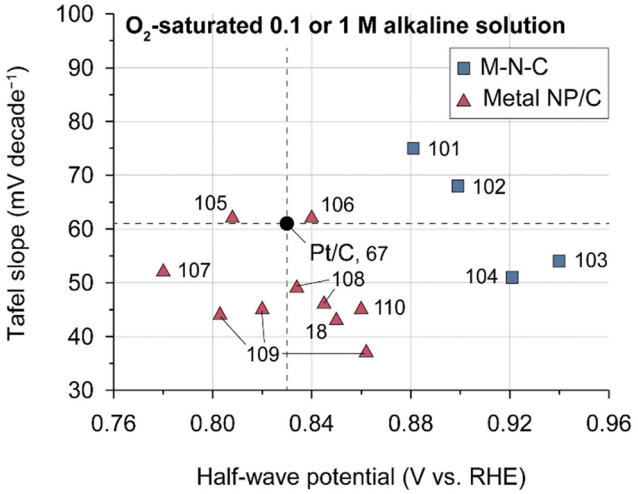

Fig. 5 ORR performances of state-of-the-art NPM catalysts. Tafel slopes and half-wave potentials of various NPM ORR catalysts. The performances were evaluated for 0.1 or 1 M aqueous alkali solution in the RDE system (Table 6).[18,67,101–110]

electron transfer process. In the case of alkaline media, electron transfer to the chemisorbed O_2 molecule *via* the inner-sphere route is the RDS, and the subsequent reactions involving supply of hydrogen from the nearby water molecules to the chemisorbed O_2 are based on inner-sphere charge transfer. However, in alkaline electrolytes, there are additional routes of outer-sphere electron transfer (mechanism 3). The molecular collisions of the hydrated O_2 molecules ($O_2\cdots(H_2O)_n$) with the adsorbed hydroxyl species lead to direct electron transfer, forming $O_2^-\cdots(H_2O)_n$. The formation of negatively charged O_2^- on the electrode surface *via* the outer-sphere pathway deviates the RDS of mechanism 2, resulting in faster ORRs in alkaline electrolytes.

Despite Pt-based catalysts exhibiting higher ORR activities under alkaline conditions compared to acidic environments, NPM catalysts have garnered more attention as ORR catalysts for AEMFCs owing to their potentially lower cost. Previous studies have reported that NPM catalysts may have higher ORR activities compared to Pt-based catalysts, presenting the possibility of replacing Pt catalysts with NPM catalysts in AEMFCs. Fig. 5 presents a comparison of the ORR Tafel slope and half-wave potentials for some recently reported NPMs and conventional Pt/C catalysts; the figure clearly shows that typical NPM catalysts have higher half-wave potentials and lower Tafel slopes for ORRs in half-cell tests, demonstrating the potential for cost-effective AEMFCs (Table 6).

Among NPM catalysts, manganese oxide-based catalysts have emerged as a promising alkaline ORR catalyst and have been a subject of intensive investigation. MnO_2 exhibits diverse crystal structures, including α, β, γ (1D-tunneled), δ (2D layered), and λ (3D spinel), and the catalytic activity varies depending on the crystal structure (δ- ≈ α- > γ- > λ- > β-MnO_2).[111,112] In the case of δ-MnO_2, cation intercalation takes place, and ORR activity changes with the type of intercalated cation.[112–114] It was found that Ni doping is effective in increasing the catalytic activity of manganese oxide catalysts.[115–117] A recent research unveiled the correlation between MnO_2 degradation and HO_2^- generation, offering valuable insights for advancing the durability of the MnO_2 catalyst.[118]

However, the high ORR activities of the NPM catalysts measured in half cells do not necessarily translate to high single-cell power performances. In a half-cell, the CL readily forms a two-phase interface of electrolyte and catalyst; therefore, the ORR activity is not highly sensitive to the CL structure, whereas in a single cell, the TPB involving the electrolyte, catalyst, and gas, which sensitively changes with the CL structure determines the power performance.

In the half-cell test with a rotating disk electrode (RDE), the current density of the ORR is less than 10 mA cm^{-2} owing to the low O_2 solubility of the liquid electrolyte. In contrast, single cells can operate at high current densities on the order of a few amperes per square centimeter because of the significant supply of O_2 gas.[119] Indeed, Riasse *et al.* demonstrated that the RDE analysis is not capable of assessing fuel cell performances beyond the high potential regime, in contrast to gas diffusion electrode (GDE) and differential cell (DC) methods.[120]

High-current-density operation is achieved only when the catalyst has enough surface area or turnover frequency (TOF). NPM catalysts suffer from low active-site densities and low TOFs, so a larger amount of catalyst is required to enable high-current-density operation. The high catalyst loading for NPM catalysts leads to additional problems; the thickness of the CL

Table 6 Half-wave potentials, Tafel slopes, and measurement conditions for the catalysts displayed in Fig. 5

Catalyst type	Half-wave potential (V *vs.* RHE)	Tafel slope (mV $decade^{-1}$)	Measurement condition	Ref.
Co–N–C	0.881	75	O_2-saturated 1 M KOH	101
Fe–N–C	0.899	68		102
Fe–N–C	0.94	54		103
$FeCl_1N_4$/CNS	0.921	51		104
Co_3O_4, Co NP/N-doped graphene	0.808	62		105
CoO NP/N-doped carbon	0.84	62		106
Fe_xN NP/N-doped graphene	0.78	52		107
$CoMn_2O_4$/C	0.834	49		108
$MnCo_2O_4$/C	0.845	46		
Ni_3N/C	0.803	44		109
Fe_3N/C	0.82	45		
Co_3N/C	0.862	37		
MnCo/C	0.85	43		18
$MnCo_2O_3$/C	0.86	45		110
Pt/C	0.83	61	O_2-saturated 0.1 M NaOH	67

becomes large, increasing the mass transport limitation due to the longer O_2 transport pathway. In addition, the thick CL increases the electron and ion pathways, causing an increase in the Ohmic resistance. NPM-based CL structures have rarely been studied, and this lack of understanding makes it difficult to design high-performance NPM CLs. A recent review[121] and related research.[122] emphasize the importance of NPM-based CL design.

4.1.3. HOR catalysts. In contrast to ORR kinetics, HOR kinetics is slower under alkaline conditions than under acidic conditions. Fig. 6a compares the exchange current densities at pH 0 and 13 for Pt/C, Ir/C, and Pd/C catalysts. Regardless of the catalyst type, the exchange current densities at pH 0 are two orders of magnitude higher than those at pH 13.[123] However, the root cause of the pH dependency is not yet fully elucidated and still under debate. Two mechanisms have been proposed for the HOR: the Tafel–Volmer and Heyrovsky–Volmer mechanisms (Fig. 6b). Both mechanisms commonly involve the Volmer reaction, which is the reduction of adsorbed hydrogen, but differ in the process of hydrogen adsorption. The Tafel reaction features adsorption of hydrogen molecules on catalysts and their dissociation into hydrogen atoms. Therefore, if the HOR follows the Tafel–Volmer mechanism, the hydrogen binding energy (HBE) of the catalyst becomes one of the key parameters determining the reaction kinetics. On the other hand, in the Heyrovsky reaction, OH^- is adsorbed first, followed by adsorption of hydrogen on the catalyst surface. In the Heyrovsky–Volmer mechanism, the HOR activity is influenced by the affinity between the catalyst and OH^- (oxophilicity of the catalyst).

Although it is still unclear which of the two reaction pathways dominate the HOR, previous studies have provided significant results supporting both mechanisms. Yan's group systematically compared the HOR activities of Pt at various pH values, demonstrating that the HOR half-wave potentials (Fig. 6c) and HOR overpotentials monotonically increase with greater HBE, supporting the Tafel–Volmer mechanism.[124] Gasteiger's group demonstrated that oxophilicity is not a critical descriptor of the HOR as Pt exhibits greater HOR activity compared to Ir and Pd at pH 13, despite having the highest oxophilicity for Ir.[123] They found that the difference in HBEs between pH 0 and 13 ($\Delta E_{binding}$ = 12.5–13.5 kJ mol^{-1}) follows the Arrhenius equation $\left(\frac{r_{pH=0}}{r_{pH=13}} \approx \exp\left[\frac{\Delta E_{binding}}{RT}\right]\right)$ and that this difference successfully explains the 120–180 times lower exchange current densities at pH 13 compared to those at pH 0 (Fig. 6a), supporting the Tafel–Volmer mechanism.

In contrast, Markovic's group observed an increase in HOR activity with increasing oxophilicity for metal catalysts (Ir > Ru > Pt).[125] Moreover, they demonstrated increased HOR kinetics by introducing $Ni(OH)_2$ nanoparticles on the Pt surface, which promotes the dissociation of water into hydrogen and hydroxyl intermediates (Fig. 6d). On the basis of their findings, they proposed that the adsorption energy of OH_{ads} could be a key descriptor of the HOR, supporting the Heyrovsky–Volmer mechanism.

Kim's group presented a different view on the HOR catalytic activity by considering the interactions between the ionomer and catalyst.[126] They suggested that the cationic groups of AEIs

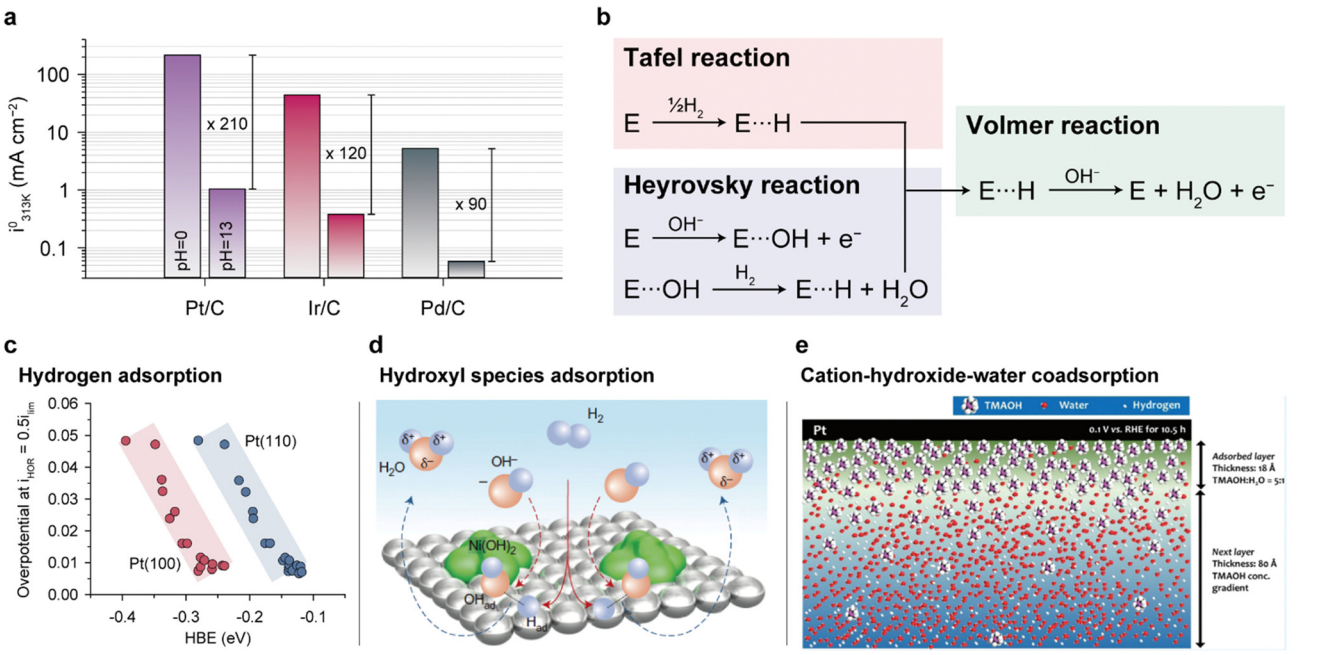

Fig. 6 HOR mechanisms and performance determinants for anode catalysts. (a) HOR/HER exchange current densities of carbon-supported Pt, Ir, and Pd at 313 K at 0 and 13 pH. (b) Two proposed HOR pathways. Three parameters governing the HOR performance: (c) hydrogen adsorption, (d) hydroxyl species adsorption, and (e) cation-hydroxide-water co-adsorption. The HOR/HER exchange current densities in (a) are reprinted with permission.[123] The half-wave overpotential *versus* HBE plot in (c) is reprinted with permission.[124] Schematic representation of the HOR process on $Ni(OH)_2$/Pt(111) in (d) and the cation–hydroxide–water co-adsorbed layer in (e) are adapted with permission.[125,126]

strongly adsorbed on the Pt catalyst surface hinder diffusion of H_2, thereby lowering the HOR activities (Fig. 6e). The HOR activity of the Pt catalyst decreases with an increase in the absorbance of the methyl peak in the infrared reflection absorption spectroscopy data, indicating the adsorption of TMA (typical cationic group of AEIs) on the Pt surface. Furthermore, neutron reflectance analysis demonstrates that when a voltage of 0.1 V *vs.* RHE is applied to the Pt catalyst in 0.1 M TMAOD/D_2O electrolyte (hydrogen is converted to deuterium in TMAOH/H_2O), an 18 Å TMA-OH-water coadsorption layer forms on the surface after 10.5 h. The high cation–hydroxide concentration in the coadsorbed layer restricts H_2 access to the catalyst surface, thereby restraining HOR activity (Fig. 6e).

HOR catalysts have received less attention in the context of AEMFCs compared to ORR catalysts owing to their higher activities. It is worth noting that Pt/C catalysts exhibit fast HOR kinetics in alkaline environments and that other precious-metal catalysts such as Ir, Pd,[127] Ru, and their alloys are not superior to the Pt-based catalysts, as demonstrated in the comparison of HOR activities among Pt/C, Ni/C, and other precious-metal catalysts (Fig. 7 and Table 7). Among NPMs, nickel-based catalysts are under active investigation for their high activity. A partially oxidized Ni surface proves to be an ideal structure for the HOR since H strongly adsorbs on Ni metal and weakly adsorbs on Ni oxide.[128,129] Various strategies including functionalization,[130] core–shell structures,[136,139] alloys ($Ni_{0.95}Cu_{0.05}$),[140] and carbon supports (carbon nanotubes (CNTs) and N, S-doped carbon),[137,138] have been employed to modify nickel-based catalysts for their use as a HOR catalyst. However, their HOR activity remains approximately two orders of magnitude lower than that of Pt/C catalysts.

Practical anode CLs in AEMFCs typically have higher precious-group metal (PGM) catalyst loadings of over 0.3 mg cm^{-2} compared to PEMFCs (<0.1 mg cm^{-2}).[6,25,45] This difference can be attributed not only to the relatively low HOR activities of PGM catalysts under alkaline conditions but also to the adsorption of AEIs on the catalysts, which is exacerbated by water flooding in the anode CLs (as described in the next section). Although PtRu/C is conventionally used instead of Pt/C because PtRu reduces the adsorption energy with AEIs more effectively than Pt,[40,141] this does not completely solve the problem of limiting H_2 diffusion caused by AEI adsorption. Therefore, while emphasizing the importance of research on non-precious metal-based HOR catalysts, it is essential to consider the problem of AEI adsorption on the precious-metal catalyst surface and the inhibition of H_2 supply due to water flooding, especially for low-loading precious-metal catalysts on the anode.

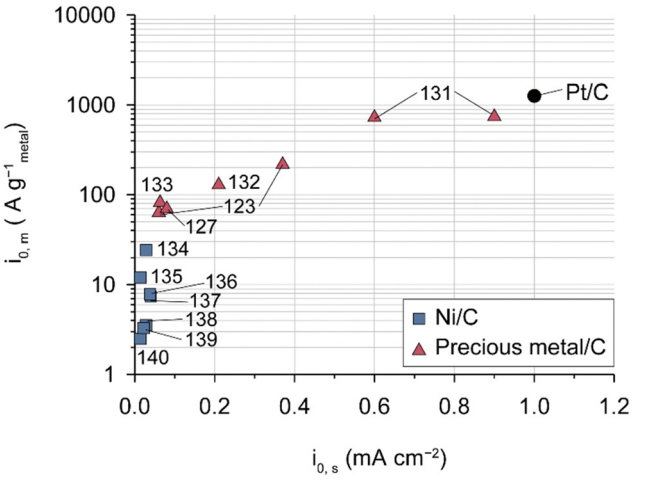

Fig. 7 HOR activities measured using the half cell with state-of-the-art catalysts. Mass- and area-specific exchange current densities of various HOR catalysts evaluated for 0.1 or 1.0 M aqueous alkali solution in a RDE system (Table 7).[123,127,131–140]

4.2. Water management

Despite the use of highly active ORR catalysts and highly conductive AEMs and AEIs, the power performances of AEMFCs are often limited by water imbalance in the MEA. This is attributed to the simultaneous water generation at the anode and water consumption at the cathode (Fig. 8a). When water cross-over from the anode to cathode is not as fast as the generation or depletion of water, the anode can become flooded and the cathode can become dried out. The difference in water content between the two electrodes increases with current or operation time, exacerbating the water flooding and drying problems. Water imbalance on both electrodes during actual AEMFC operation has been observed using neutron beams (Fig. 8b) or synchrotron X-rays (Fig. 8c). While this issue also occurs in PEMFCs, it is not as significant as that in AEMFCs owing to their different stoichiometries; in PEMFCs, two water molecules are generated per four electrons ($O_2 + 4H^+ + 4e^- \rightarrow 2H_2O$), whereas in AEMFCs, four water molecules are generated per four electrons ($2H_2 + 4OH^- \rightarrow 4H_2O + 4e^-$). Therefore, at a fixed current density, the water generation rate at the AEMFC anode is two times faster than that at the PEMFC cathode. Additionally, water consumption at the cathode exacerbates the water imbalance.

Water imbalance in the MEA causes serious problems; flooded water fills the interstitial pores in the anode CL, blocking the supply of H_2 molecules to the catalyst surface. Besides, the swelling of the AEI phase in the anode CL leads to pore clogging, which worsens the H_2 transport problem. While the water depletion at the cathode CL can facilitate diffusion of O_2 molecules, drying of the cathode leads to increased Ohmic resistance due to the ionic conductivity loss of the AEI binder. The mass transport resistance of the cathode CL can be augmented because of the limited supply of H_2O.

Various attempts have been made to achieve balanced water distribution within the MEA. Peng *et al.* showed that the cell performance can be dramatically improved by systematically controlling the temperature of the cell and humidifier.[8] On the left side of Fig. 9a, the micro-X-ray computed tomography images of an anode CL at open-circuit voltage (OCV, upper) and at a current density of 0.2 A cm^{-2} (lower) are compared. This technique enables real-time observation of the internal structural changes of the CL during cell operation. When a current of 0.2 A cm^{-2} was applied, the pores inside the CL, which initially appeared as dark regions, became bright.

Table 7 Specific exchange current density, mass exchange current density, and measurement conditions for the catalysts displayed in Fig. 7

Catalyst type	Specific exchange current density (mA cm^{-2})	Mass exchange current density (A g_{metal}^{-1})	Activity measured environment	Ref.
Ir_3PdRu_6/C	0.9	740	H_2-saturated 0.1 M KOH	131
Ir_9Ru/C	0.6	728		
Ir/C	0.37	218	0.1 M NaOH, $p_{H_2} \approx 100$ kPa_{abs}	123
Pd/C	0.06	63		
Pd/C	0.08	70.5	H_2-saturated 0.1 M KOH	127
Ir/C	0.21	128.6		132
Ru/C	0.063	82	H_2-saturated 0.1 M NaOH	133
Ni/C	0.028	24.41	H_2-saturated 0.1 M KOH	134
Ni_3N/C	0.014	12		135
Ni (core)@N-doped carbon (shell)/C	0.038	7.84		136
Ni/S-doped C	0.04	7.4		137
Ni/N-doped CNT	0.028	3.54		138
Ni (core) @boron nitride (shell)/C	0.022	3.3	H_2-saturated 0.1 M NaOH	139
$Ni_{0.95}Cu_{0.05}/C$	0.014	2.5		140

These results demonstrate the swelling of AEI binders during cell operation and clogging of the pores between the Pt/C particles. To inhibit excess ionomer swelling, the RH of the anode feed was lowered, and a 3-fold increase in the entire range of current densities of the AEMFC was achieved (right side of Fig. 9a).

Another approach to mitigate water imbalance is controlling the hydrophobicity of the CL. Hyun *et al.* introduced oxygen- and fluorine-functionalized carbon additives in the CL to produce hydrophilic and hydrophobic CLs, respectively.[143] They observed water condensation on the CL surfaces using environmental scanning electron microscopy (SEM). As shown in Fig. 9b, the hydrophilic CL surface was wet or partly covered with water droplets with very small contact angles (upper), which is in contrast to water droplets with large contact angles formed on the hydrophobic CL surface (lower). The hydrophobicity-controlled MEA paired with the hydrophilic cathode CL and hydrophobic anode CL showed higher current densities compared to the control MEA and alleviated the limiting current behaviors in the high-current-density regime (Fig. 9b). These results suggest that the hydrophilic CL retains water and that the hydrophobic CL drains water, thus mitigating the water imbalance.

The water imbalance can also be reduced by introducing a membrane with high water flux. During cell operation, the accumulated water in the anode CL diffuses to the cathode because of a concentration gradient, which is denoted as "water back-diffusion" (upper left in Fig. 9c). The water back-diffusion is facilitated using a membrane with higher diffusivity. Accordingly, a polynorbornene-based AEM with high water diffusivity resulted in superior power performance. Mandal *et al.* decreased the thickness of the polynorbornene-based AEM using light cross-linking with the hexyl spacer diamine (1 of Fig. 3b).[97] As the membrane thickness decreased, the water flux across the membrane increased exponentially (lower left in Fig. 9c).[144] As shown on the right side of Fig. 9c, the power performance was enhanced with decreasing membrane thickness, and by using a 10 μm-thick AEM, a current density exceeding 6 A cm^{-2} was achieved.

Recently, a self-regulating anode CL was suggested by Zhang *et al.* for better water management at the anode.[145] PtRu/C catalysts have a tendency to aggregate more than Pt/C, resulting in the formation of a larger pore structure when used as a CL. The researchers combined PtRu/C and Pt/C CLs into one anode CL with distinct layers, creating smaller pores from the gas diffusion layer to the AEM. The CLs with this gradient nanopore structure exhibit efficient water transport through the capillary effect. They were characterized by rapid moisture drainage even under high humidity conditions and demonstrated high power performance at 100% RH.

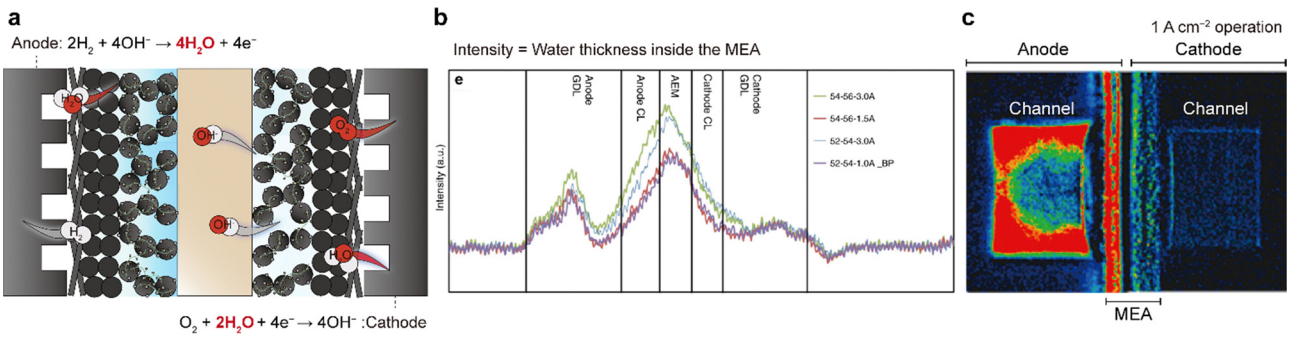

Fig. 8 Water imbalance issue in AEMFCs. (a) Schematic of water flooding at the anode and drying out at the cathode. (b) Water distribution plots inside the MEA extracted from high-resolution neutron radiographic images. (c) *In situ* synchrotron X-ray colored images during single-cell operation using the constant current mode at 1 A cm^{-2} under fully wetted conditions. The water density decreases from red to blue. Panels (b) and (c) are reprinted with permission.[8,142]

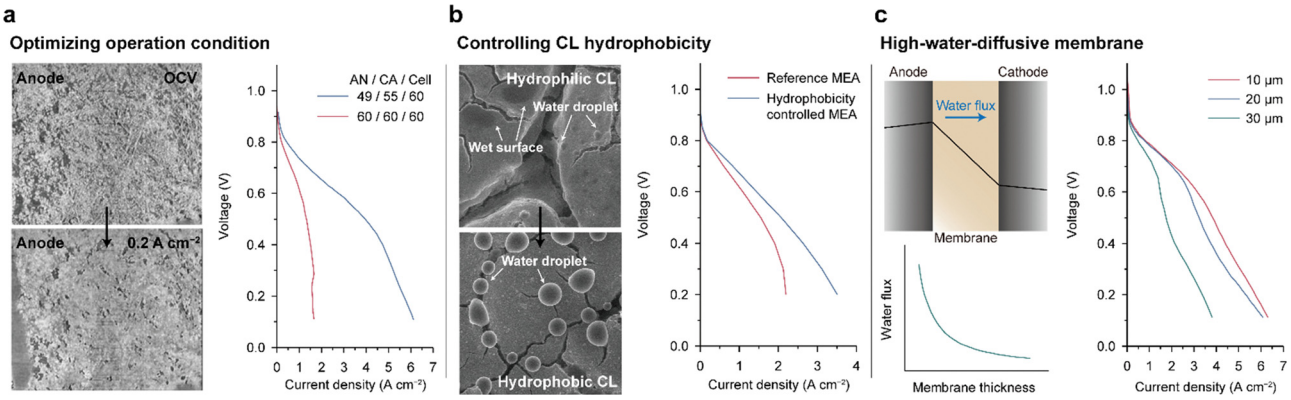

Fig. 9 Strategies for mitigating water imbalance. (a) Operando micro-X-ray computed tomography scans of the interface between the gas diffusion layer and CL of PtRu/C anodes at open-circuit voltage (OCV) (left upper) and 0.2 A cm^{-2} (left lower) under 100% RH. The *i*–*V* curves of the fully humidified and optimal humid conditions are displayed on the right. (b) SEM images of the CL surfaces containing a hydrophilic (left upper) and a hydrophobic (left lower) carbon additive under fully humidified conditions. The *i*–*V* curves of the control and optimal MEAs paired with the hydrophobic anode CL and hydrophilic cathode CL (right). (c) Predicted water distribution and direction of water flux inside the MEA during cell operation (left upper), water flux *versus* membrane thickness plot (left lower), and three *i*–*V* curves for MEAs with different membrane thicknesses (right). Panels (a) and (b) are adapted with permission.[8,143] The water flux plot and *i*–*V* curves in (c) are reprinted from ref. 144 and 97, respectively.

The significance of regulating water distribution within the MEA is apparent from its substantial influence on the cell performance. However, in practical applications like light-duty vehicles, where the distribution of water in the MEA changes rapidly due to the dynamic operating conditions, prompt responses are essential. Thus, a more dynamic evaluation method that models real driving conditions beyond the *i*–*V* polarization curve and incorporates material development with MEA design is necessary.

Additionally, the water distribution within the CL significantly impacts the durability of AEMFC as reported previously.[146] The performance loss of AEMFCs can be classified into two categories: recoverable loss and permanent loss. The former arises from temporary limitation in H_2 (anode) and OH^- (cathode) supply caused by water flooding and water drying, respectively. When the water shortage in cathode exacerbates, the OH^- concentration in cathode increases, leading to the degradation of the cation group in the AEI (further details are provided in Section 5.2.2). Notably, Hyun *et al.* demonstrated that mitigating water imbalance through carbon modifications can help achieve stable operation for 1000 h, which is in contrast to the short lifetime (200 h) of the control MEA.[143] Various carbon modification methods including fluorination[11] can be used in this approach.

4.3. CO_2 poisoning

CO_2 poisoning is the most critical problem of an AEMFC from the practical aspect. CO_2 can chemically react with OH^-, forming carbonate species (note the equations in Fig. 10a). The carbonate formation reaction occurs spontaneously and is quite fast; merely 400 ppm of CO_2 from ambient air can significantly lower the OH^- concentration in the AEM and AEI. Accumulation of the carbonate species greatly reduces the AEMFC performance or destabilizes the OCV. CO_2 poisoning essentially complicates the manufacturing process of the AEMFC. Before cell assembly, AEM- and AEI-containing CLs should be submerged in an alkaline solution to replace the carbonate anions with OH^-. However, despite these efforts, the AEM and CLs are inevitably exposed to CO_2 again during single-cell assembly.

CO_2 poisoning also makes cell operation with ambient air challenging. As shown in Fig. 10a, the CO_2 injected into the cathode reacts with the OH^- of the AEI in the CL and is converted to CO_3^{2-}. The carbonate species migrates from the cathode to anode driven by the electric field and accumulates at the anode CL. Some carbonate species are also reconverted to CO_2 and emitted. If the AEMFC is operated under a constant

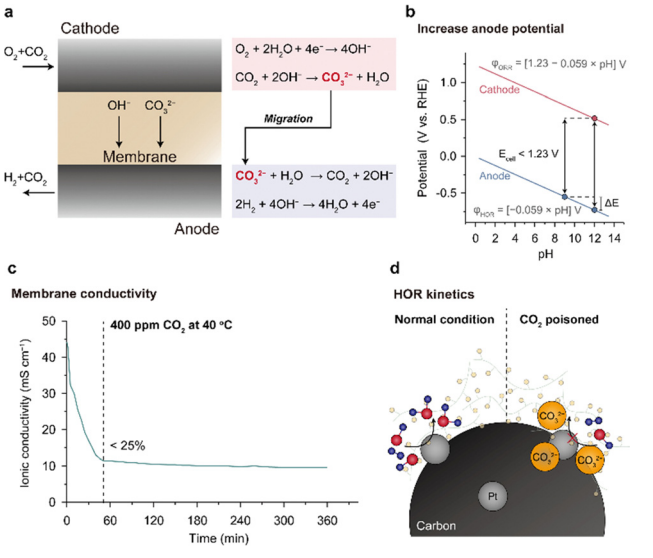

Fig. 10 CO_2 poisoning in AEMFCs. (a) Carbonate species formation and removal processes at the cathode and anode. Three reasons for AEMFC performance degradation due to CO_2 poisoning: (b) reduced cell voltage by increase of anode potential, (c) decreased ionic conductivity of the membrane by carbonate species formation, and (d) kinetic loss in the HOR due to blocking of the catalyst surface by the carbonate species. The plot for ionic conductivity *versus* time is reprinted with permission.[147]

voltage with constant reactant gas flow, the carbonate concentrations of the cathode, membrane, and anode CL can converge to steady-state values. However, CO_2 poisoning is hard to control in dynamic operations, often leading to a local increase in the carbonate concentration in the MEA. This means that sophisticated power control is required for AEMFCs used in transportation applications.

The carbonate species in the MEA decreases the performance of the AEMFC in three ways: (1) increasing the anode potential, (2) decreasing the ionic conductivity of the AEM, and (3) decreasing the HOR kinetics of the anode catalyst. In the absence of CO_2 in the AEMFC, it can be assumed that both the anode and cathode have the same pH and that the theoretical voltage is 1.23 V (Fig. 10b). However, when CO_2 poisoning starts and the carbonate species accumulate at the anode, the pH of the anode becomes lower than that of the cathode. Since the potential of the anode decreases linearly with pH, the theoretical voltage of the AEMFC decreases (<1.23 V). For this reason, when the AEMFC is assembled under ambient air, its OCV is often low and unstable.

The ionic conductivity of the AEM is decreased by carbonate formation because of the reduced OH^- concentration in the AEM. OH^- molecules can migrate rapidly in the AEM under an electric field *via* the Grotthuss mechanism, whereas the migration of CO_3^{2-} molecules is slower than that of OH^- because they does not migrate *via* the Grotthuss mechanism but through the vehicle mechanism. As shown in Fig. 10c, the ionic conductivity of the AEM decreases exponentially to 25% of the initial value within 1 h when exposed to ambient air. Under the cell operating environment, the ionic conductivity of the AEM is not expected to be significantly reduced because the carbonate species are removed from the anode. However, in the idle mode, when the MEA is exposed to the atmosphere, carbonate species will be readily generated inside the AEM and AEI, causing rapid performance degradation upon restart.

The last negative effect of CO_2 poisoning on AEMFC performance is reduction of HOR catalyst activity (Fig. 10d). The high concentration of carbonate species near the HOR catalyst surface may block the access of OH^- to the surface of the HOR catalyst and increase the charge transfer resistance.[148,149] Although there are no studies reporting the direct measurement of charge transfer resistance, Mustain's group was able to derive it by setting up an environment that can neglect the resistive component from the cathode ORR side and by subtracting the Nernst voltage loss due to the pH increase of the anode and Ohmic overvoltage from the total voltage drop on the anode side.[148]

Various approaches have been attempted to suppress carbonate formation. Mustain's group controlled various operation parameters of the AEMFC (current density, temperature, and anode/cathode feed flow rate) as well as conducted electrochemical analyses and real-time probing of CO_2 emissions from the cathode and anode. With increasing current density, the Ohmic resistance of the AEM reduced, indicating reduced CO_2 in the MEA (1 of Fig. 11a). This was supported by the increased CO_2 concentration in the anode exhaust and decreased CO_2 concentration in the cathode exhaust. Increasing the cell temperature also mitigates CO_2 poisoning. With increasing temperature, the solubility of CO_2 in water decreases, the conversion rate of carbonate to CO_2 increases, and the transportation of CO_2 and OH^- become easier. Owing to these combined effects, the cell overpotential caused by CO_2 decreases with temperature (2 of Fig. 11a). The flow rate of the feed gas also impacts carbonation in a cell. The CO_2 overpotential decreases with the flow rate of the anode feed (3 of Fig. 11a), whereas it increases with the flow rate of the cathode feed (4 of Fig. 11a). Intuitively, a higher flow rate of the anode gas can release CO_2 more efficiently from the cell, and a higher flow rate of the cathode gas will lead to increased amount of CO_2 entering the cell, resulting in more significant carbonation. In addition, the hydration level of the cell affects CO_2 poisoning.[149] Increasing the amount of water inside the cathode reduces the basicity of the electrolyte in the CL, which leads to a decrease in CO_2 solubility. Under optimized conditions, the AEMFC shows a stable *i–V* polarization curve without any catastrophic voltage losses.

The fine-tuning of the operating environment of the AEMFC could significantly mitigate carbonation inside the MEA; however, it is not compatible with dynamic operations of practical fuel cells. Instead, CO_2 scrubbing systems are more effective and straightforward for solving the carbonation problem. The currently available CO_2 capture systems are mostly based on reversible CO_2 adsorption and desorption on absorbent materials with a regeneration process.[152,153] However, this type of chemical CO_2 scrubbing is hard to combine with AEMFC systems because of the insufficient CO_2 adsorption capacity and time-consuming regeneration step. Therefore, in the AEMFC technology sector, an electrochemically driven CO_2 scrubbing system that can continuously remove CO_2 has attracted interest.

One approach is using the sub-AEMFC as a CO_2 filter. The overall configuration is shown at the top of Fig. 11b; the cathode outlet of the sub-AEMFC is connected to the cathode inlet of the main AEMFC, and the anode outlet of the main AEMFC is connected to the anode inlet of the sub-AEMFC. The CO_2-free effluent from the sub-AEMFC is supplied to the main AEMFC, and the residual H_2 from the main AEMFC is injected into the sub-AEMFC. The reactions in the sub-AEMFC are identical to those in the main AEMFC, as described in Fig. 10a. The CO_2 from the atmosphere combines with OH^- to form carbonate anions at the cathode of the sub-AEMFC. The carbonate anions are transported to the anode, converted to CO_2, and released into the atmosphere with the anode effluent. Zheng *et al.* implemented a pair of sub- and main-AEMFC systems and demonstrated that a sub-AEMFC with a size of 5 cm^2 can reduce the CO_2 concentration from 400 to 240 ppm.[150] The 25 cm^2 sub-AEMFC can operate for over 150 h with less than 100 ppm CO_2 emission (upper right of Fig. 11b). Furthermore, they showed that the main AEMFC exhibits the same *i–V* polarization curves when tested with CO_2-free air and the exhaust from a 50 cm^2 sub-AEMFC that operates under ambient air.

Another approach is adopting an electrochemically driven CO_2 separator (EDCS) developed by Yan's group.[151] The EDCS is based on carbonate chemistry similar to the sub-AEMFC, but it

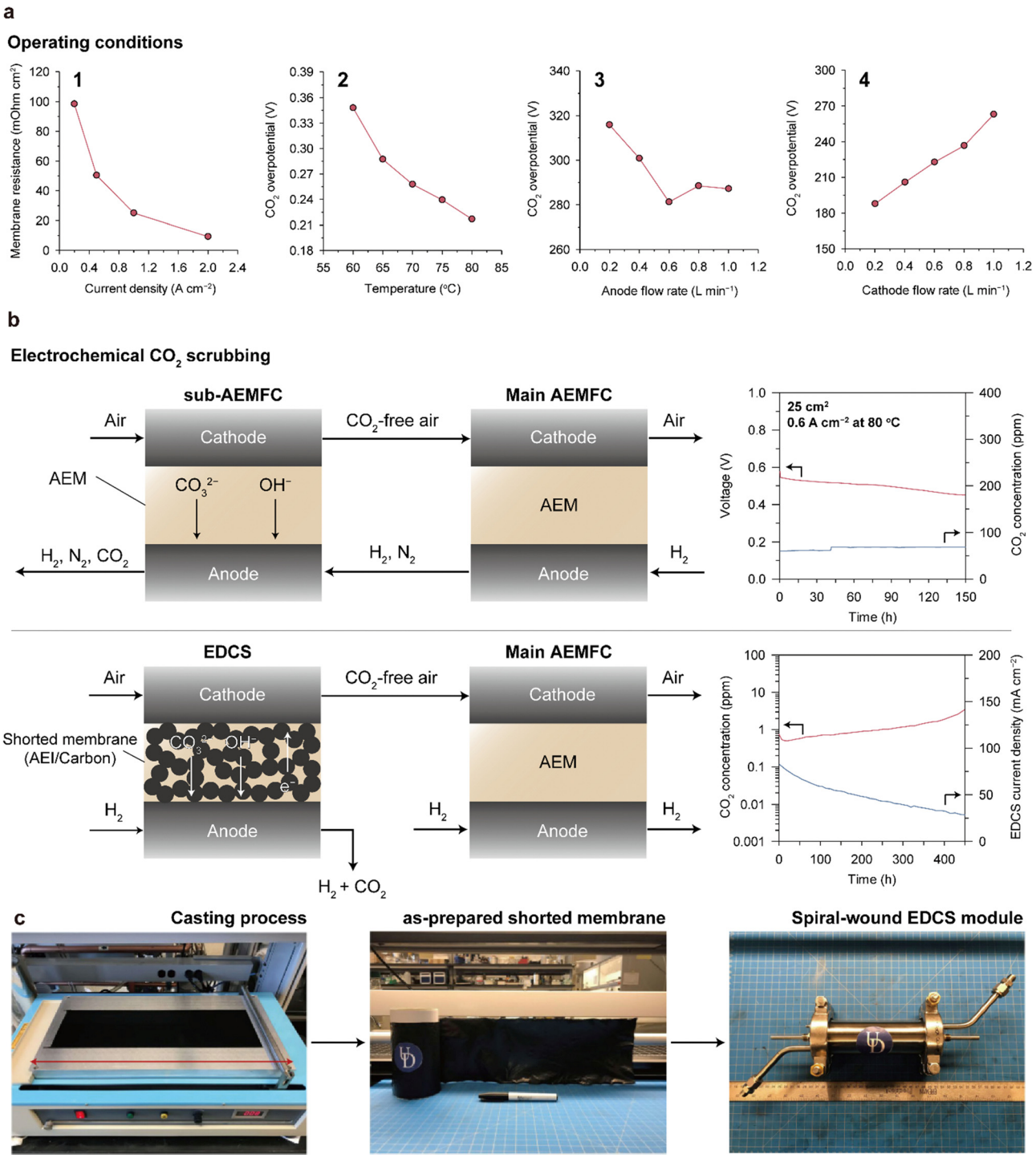

Fig. 11 Strategies for mitigating CO_2 poisoning. (a) Change in membrane resistance or CO_2 overpotential with adjustment of the operating conditions, including current density, temperature, anode feed flow rate, and cathode feed flow rate (reprinted with permission from ref. 148 and 149). (b) Structure and durability of the sub-AEMFC (top)[150] and EDCS (bottom)[151] as an electrochemical CO_2 scrubbing system. (c) Overall fabrication process of the spiral-wound EDCS module. Bottom of panels (b) and (c) are adapted with permission from ref. 151.

employs a shorted membrane to induce internal current. The shorted membrane comprising carbon and AEIs enables transport of anions (OH^- and carbonate species) and electrons concurrently. The internal shorting accelerates the ORR and HOR in the EDCS, enhancing the efficiency of CO_2 removal from the cathode air feed. The filtering ability of the EDCS is remarkable; it can lower the CO_2 concentration in the air feed at 1000 sccm from 400 to <1 ppm using only 5 sccm of H_2 gas. Moreover, the EDCS showed 99% CO_2 removal capacity for 450 h (lower right of Fig. 11b). The strong advantage of the

EDCS is that it does not require any external circuitry and the degree of CO_2 removal from the air feed can be adjusted by varying the flow rate of the H_2 injected into the EDCS. Furthermore, both the cast-made shorted membrane and spiral-wound configurations of the EDCS (Fig. 11c) are compatible with conventional manufacturing processes, thereby increasing the practicality of the EDCS. However, EDCS inevitably consumes a certain amount of hydrogen, which decreases fuel efficiency; system level energy efficiency should be studied in more detail.

As described in this section, the injection of CO_2 causes catastrophic performance loss to the AEMFC. Therefore, this problem must be resolved before using the AEMFC as a power source.[65,154] However, CO_2 removal technology is a long-standing challenge that has not been completely solved in other electrochemical devices, such as zinc–air and Li–air batteries, and the complex carbonate chemistry increases the difficulty of research. Nevertheless, the sub-AEMFC and EDCS are promising candidates for CO_2 removal systems, and their further research is encouraged. In addition, membrane CO_2 filtration can be a viable option to consider.[155] Alongside the infiltration of CO_2 from outside into AEMFCs, CO_2 can be generated inside the MEA *via* electrochemical oxidation of carbon materials. This issue cannot be fully addressed even when a CO_2 scrubbing system is employed. Therefore, it should be also considered for achieving long-term operation of AEMFCs.

4.4. MEA design

The HOR and ORR occur at electrochemically active surface areas (ECSAs) of the catalyst surfaces where the transportation of electrons, ions, and molecules (reactants, and products) is available, conventionally denoted as TPB. Since a thin ionomer layer in contact with the catalysts enables the passage of ions and molecules, the two-phase interface of the ionomer/catalyst can form a TPB with pores and serve as an ECSA. To improve the performance of the AEMFC with a limited amount of catalyst, the ECSA should be augmented. Therefore, a CL design that directs uniform ionomer distribution and a porous CL structure is required. In the case of nonuniform ionomer distribution, locally concentrated ionomers on the catalyst surface block the access of reaction gases and also result in electrically isolated catalysts. In addition, the ionomer-deficient portion of the CL limits the migration of OH^- ions. Since the reactant and product gases pass through the pores of the CL, it should have high porosity for facile mass transport. In addition to porosity, the size of the pores is also important. Small pores can cause water flooding, which restricts gas access, and pores that are too large reduce the connectivity of the CL. Designing an optimal CL poses a formidable challenge as it necessitates satisfying multiple conditions concurrently. Detailed discussions on this topic can be found in recent comprehensive reviews.[156,157]

Only a few studies have been conducted on the CL structure of the AEMFC despite its importance. Carlson *et al.* changed the CL structure by varying the ionomer–Pt/C ratio to 0.2, 0.6, and 1.0 and analyzing the cell performances comparatively.[158] The SEM images of the CL surfaces varied with the ionomer content, as shown on the left side of Fig. 12a. As the ionomer content increased, the pores disappeared, and a thick ionomer film was observed at a ratio of 1.0. The highest cell performance was achieved at an intermediate ratio of 0.6 because an adequate amount of ionomer ensures facile ion and mass transport. The CL with a lower ionomer content (0.2) has the lowest performance due to limited OH^- transport in the CL. At a higher ratio of 1.0, the thick ionomer film hinders the reactant molecules from reaching the catalyst surface, limiting the cell performance, as indicated by the large overpotential in the high-current regime. The ionomer content is a critical design parameter that determines CL performance, and it should be carefully adjusted considering the interplay between ionomer and catalyst materials. The optimal ionomer content should vary depending on the size and surface properties of the catalysts because the catalyst surface area–ionomer volume ratio and ionomer–catalyst interaction influence the ionomer distribution and pore structure of the CL. Moreover, the influence of ionomer content on mass transport may change depending on the hydrophilicity of catalyst particles. When the catalyst is prone to water flooding, ionomer content needs to be reduced to provide sufficient interstitial pore volume. Understanding of the ionomer–catalyst interaction and the consequent CL structure is necessary to advance AEMFC CL technology.

Hyun *et al.* investigated the effects of the solvent of ionomer dispersion on controlling the CL structure and demonstrated the correlation between the resulting CL structure and cell performance.[36] The size of the ionomer aggregate in dispersion can be controlled by adjusting the ionomer–solvent interactions (Fig. 12b). If the ionomer–solvent interactions are weaker than the ionomer–ionomer interactions, the ionomer chains tend to aggregate. In contrast, stronger ionomer–solvent interactions disperse the ionomer aggregates to smaller dimensions. They found that the aggregate size of the QPC-TMA (poly(9-(6-(trimethylammoniumbromide)-hexyl)-9*H*-carbazole-*co*-1,1,1-trifluoroisopropane)) AEI in dispersion could be decreased in the order of isopropanol (IPA) > methanol (MeOH) > dimethylsulfoxide (DMSO). As shown in Fig. 12b, the DMSO-based CL has a uniform and porous structure, whereas the MeOH- and IPA-based CLs show clumpy ionomer aggregates on the surface and pore clogging, indicating nonuniform ionomer distribution in the CLs. The power performance was enhanced by increasing the uniformity of ionomer distribution. This study also established a strong correlation between the ECSA and power performance.

5. Challenges and solutions for improving AEMFC durability

To achieve long-lasting AEMFCs, it is crucial that the materials used in the MEA exhibit chemical, mechanical, and electrochemical stabilities under operating conditions. Furthermore, the various layers and interfaces in AEMFCs must possess mechanical robustness. To date, research has primarily focused on the durability of materials, with limited studies conducted on the mechanical durability of CLs or diffusion layers, and on

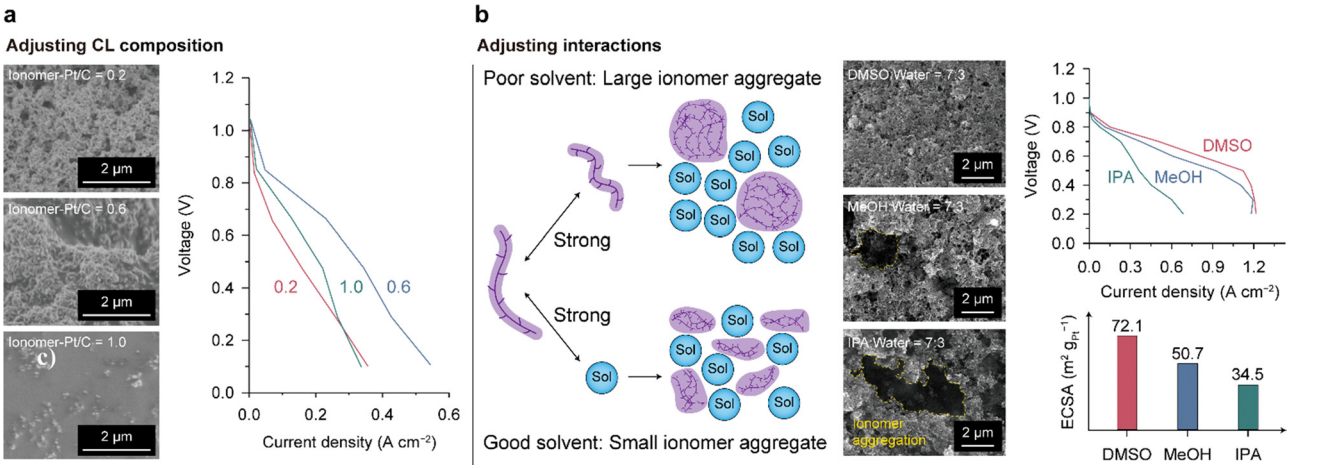

Fig. 12 Structural control of the AEMFC CL. (a) Adjustment of the ionomer content: surface SEM images of the CLs with different ionomer contents (ionomer-Pt/C ratio of 0.2 (top), 0.6 (middle), and 1.0 (bottom)) and comparison of the *i*–*V* polarization curves of the CLs. (b) Adjustment of the interactions between the ionomer and solvent: schematic of the size of ionomer aggregates in dispersion according to ionomer–solvent interaction, surface SEM images of the CLs fabricated with different solvents (DMSO (top), MeOH (middle), and IPA (bottom)), *i*–*V* polarization curves, and ECSA values for the CLs. Data in (a) and (b) are reprinted with permission from ref. 36 and 156, respectively.

the degradation or failure modes of stacks or systems. This section provides a summary of the degradation modes of the materials, describes the resulting decline in MEA performance, and discusses the underlying mechanisms and strategies to address these issues.

5.1. Catalysts

5.1.1. Pt catalysts. The Pourbaix diagram of Pt (Fig. 13a) shows that Pt exists as PtO in the ORR potential range in higher pH environments. This implies that the Pt inside the MEA of AEMFCs remains stable even during cell operation. However, according to the results of Chatenet's group, the carbon-supported Pt severely degrades in an alkaline environment. The ECSA of Pt/C decreased by 57% after 150 cyclic voltammetry (CV) cycles in a 0.1 M NaOH solution (Fig. 13b), while it decreased by 17% and 22% in 0.1 M $HClO_4$ and 0.1 M H_2SO_4 solutions, respectively.[160] TEM images of the Pt/C catalyst after CV cycling in 0.1 M NaOH demonstrate the detachment of Pt nanoparticles from the carbon support.

In their subsequent work, Chatenet's group discovered the formation of carbonate species on the Pt/C catalyst during voltage cycling.[161,164] Fig. 13c shows the Fourier-transform infrared (FTIR) spectra of the Pt/C surface, which change with voltage cycling in a 0.1 M NaOH solution. The bands at 1310 and 1390 cm^{-1} are assigned to carbonate ions (CO_3^{2-}) and bicarbonate ions (HCO_3^-), respectively, and the bands at 1610 and 1730 cm^{-1} are linked to the oxygen-containing surface groups on carbon. The intensities of these four FTIR bands increase over the CV cycles (Fig. 13c), which suggests the formation of oxygen groups on the carbon support and carbonate species on the Pt/C surface. Based on this finding, they suggested that Pt detachment from the carbon support is the major degradation mechanism of Pt/C catalysts in alkaline solutions, as shown in Fig. 13d. The Pt/C stably exists under <0.2 V potential. When the potential gradually increases, carbon corrosion/functionalization starts occurring in the 0.2–0.6 V potential range, and CO and/or COH molecules are adsorbed on the Pt surface through back spillover. Over 0.6 V, the OH molecules are adsorbed subsequently because of the positive charge and/or oxidization of the Pt. Then, Pt-adsorbed CO and OH react together and form CO_2 ($Pt\cdots CO_{ads} + Pt\cdots OH_{ads} + OH^- \rightarrow CO_2 + H_2O + 2Pt + e^-$). Another scenario for CO_2 formation is that the functional group on the carbon support directly reacts with the Pt-adsorbed OH ($C_n\cdots CO_{ads} + Pt\cdots OH_{ads} + OH^- \rightarrow CO_2 + H_2O + Pt + C_n + e^-$). As a final step, the CO_2 molecules chemically react with OH^- to form carbonate precipitates, such as Na_2CO_3 on the Pt/C surface, releasing Pt from the carbon support.

Lafforgue *et al.* investigated the stability of the Pt/C catalyst surrounded by the AEM phase using transmission electron microscopy (TEM) analysis.[162] In this work, the Pt/C and AEM-containing ink were deposited on a Lacey-carbon TEM gold grid, which served as both a working electrode and platform for TEM observations. Note that accelerated stress testing (AST) was conducted in a "dry cell", where the electrolyte consists of only a solid AEM. In contrast to the significant loss of ECSA (65%) observed for Pt/C exposed to 0.1 M NaOH solution, Pt/C surrounded by the AEM exhibited only a 13% ECSA loss after 150 cycles of CV (as illustrated in Fig. 13e). As depicted in Fig. 13f, Pt detachment did not occur significantly; instead, minor Ostwald ripening occurred in Pt/C under the AEM environment. In a liquid environment, detached or dissolved Pt can be washed away from its location, but in a solid AEM environment, it can stay around and redeposit onto Pt/C (as depicted in Fig. 13g). Additionally, even if carbonate ions are formed, precipitates do not form because they pair with the cationic groups of the AEM.

Only a few research groups have reported the stability of the Pt/C cathode and PtRu/C anode catalysts under actual operation in AEMFCs. One such study by Hassan *et al.* revealed that after 2000 h of constant current operation at 0.6 A cm^{-2}, Pt nanoparticles in the cathode were severely agglomerated (Fig. 13h).[6] Hyun *et al.* also found that Pt nanoparticles in the cathode had aggregated to form worm-like shapes after operating for 125 h at

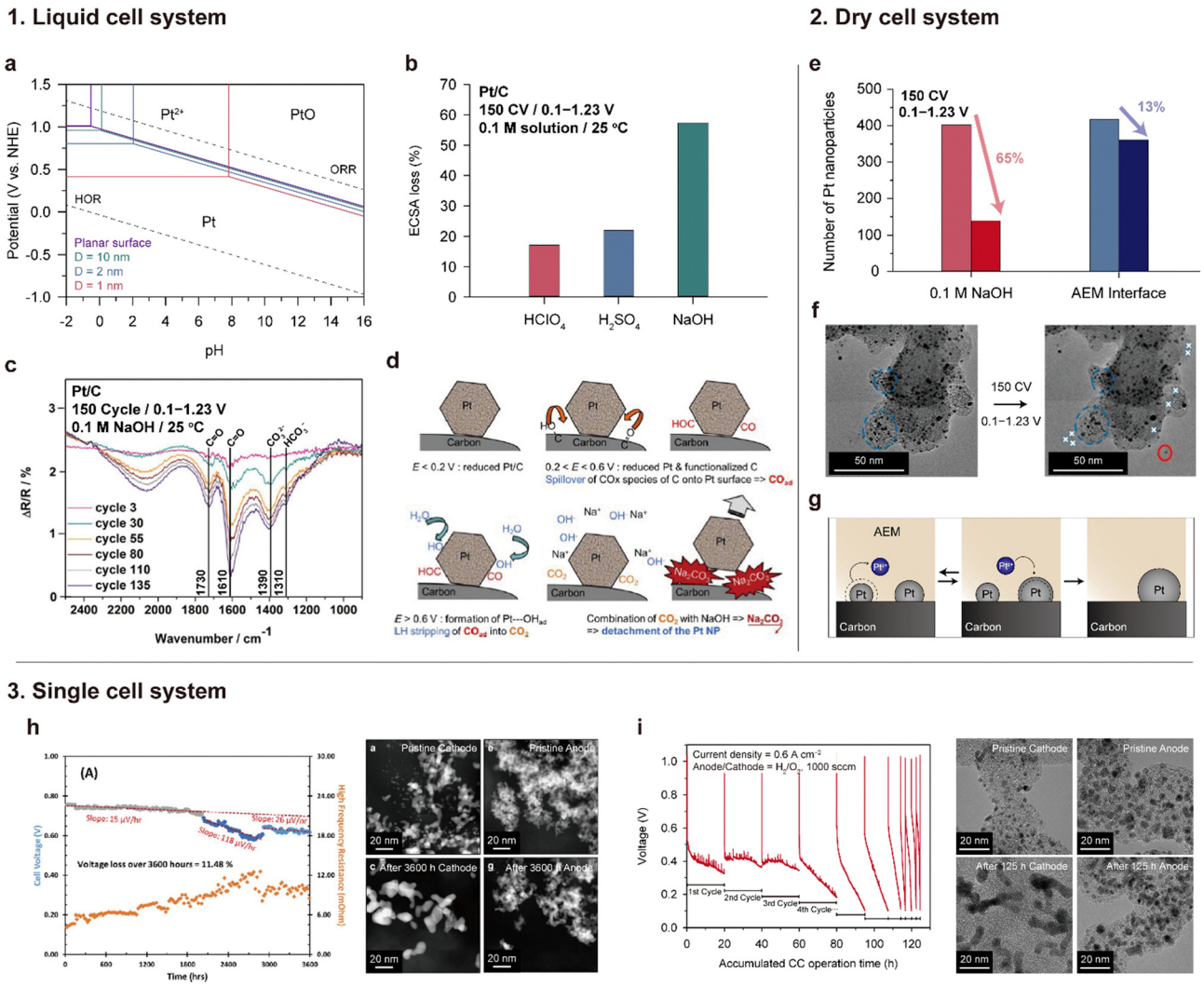

Fig. 13 Degradation of the Pt/C catalyst under alkaline conditions. 1. Severe Pt detachment in an alkaline solution: (a) Pourbaix diagram of Pt for different sizes. (b) ECSA loss after 150 CV in various 0.1 M aqueous solutions (CV is performed in the RDE setup at room temperature, and the voltage range is 0.1–0.23 V *vs.* RHE). (c) Fourier-transform infrared (FTIR) spectrum of the Pt/C catalyst after 150 voltage cycles in the range of 0.1–1.23 V *vs.* RHE in a 0.1 M NaOH at room temperature. (d) Pt detachment mechanism in an alkaline solution. Panel (a) is adapted with permission from ref. 159. Panels (b), (c), and (d) are reprinted with permission from ref. 160 and 161. 2. Ostwald ripening of Pt at the interface with an AEM. (e) Number of Pt NPs after 150 voltage cycles in 0.1 M NaOH and an AEM/CL interface. (f) TEM images before and after the degradation test. (g) Ostwald ripening and redeposition of Pt at the AEM interface. Panels (e) and (f) are adapted with permission from ref. 162. 3. Pt degradation in a single cell. (h) and (i) Voltage profiles during 0.6 A cm^{-2} of constant current operation (left) and TEM images of the cathode (Pt/C) and anode (PtRu/C) catalysts before and after durability tests (right). Panels (h) and (i) are reprinted with permission from ref. 6 and 163.

a current density of 0.6 A cm^{-2} (Fig. 13i).[163] In contrast to Pt/C catalysts, PtRu/C catalysts used in the anode CL did not exhibit any aggregation in both studies.

5.1.2. Fe–N–C catalysts. As described in Section 4.1.2., the NPM catalysts have shown good performance in alkaline AEMFC systems. Among the NPM catalysts, the most studied and promising catalyst is Fe–N–C owing to its potential for high ORR activity and low price. Despite the advantages, the biggest obstacle to its practical use is its poor durability. Previous assessments of the stability of Fe–N–C catalysts have been conducted in acidic environments because these works were intended to replace expensive Pt/C catalysts with Fe–N–C catalysts in PEMFCs. Numerous degradation pathways under acidic conditions have been noted to date, which can be classified into the following four mechanisms: demetalation,[166] surface oxidation,[165,169] agglomeration,[170] and protonation of nitrogen[171] (Fig. 14a).

Owing to the recent interest in the use of NPM catalysts for AEMFCs, the durability of Fe–N–C-based catalysts in alkaline environments is being investigated. Bae and Chung *et al.* demonstrated that the Fe–N–C catalyst is more stable in an alkaline environment than in an acidic environment.[165] The stability was assessed by monitoring changes in the half-wave potential for ORRs after H_2O_2 treatment. As shown on the left side of Fig. 14b, the change in the half-wave potential was smaller at higher pH. Under acidic conditions, H_2O_2 that is formed *via* the two-electron pathway of ORR reacts with Fe^{2+}

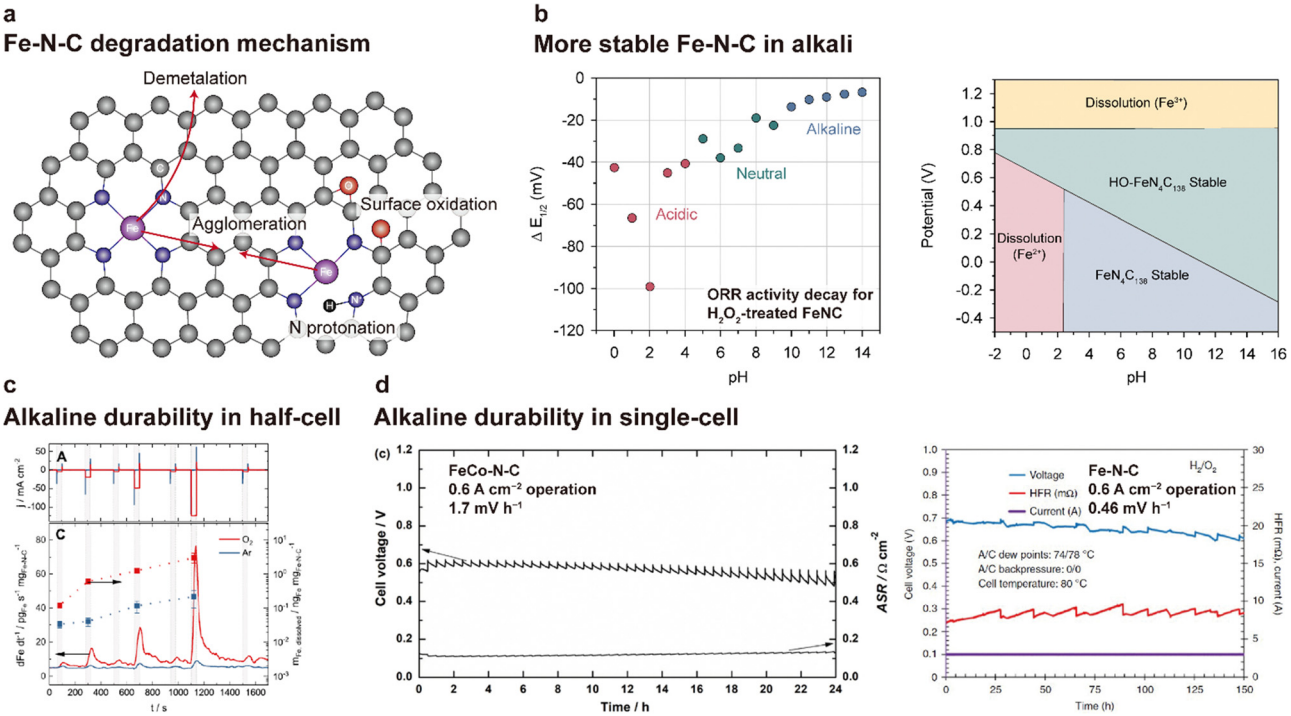

Fig. 14 Degradation of Fe–N–C catalysts in alkaline media. (a) Schematic of the degradation mechanism of the Fe–N–C catalyst. (b) Difference in $E_{1/2}$ values of the Fe–N–C catalyst before and after H_2O_2 treatment (left). H_2O_2 treatment was conducted in a pH-adjusted solution containing 1 wt% H_2O_2 for 2 h at 50 °C. Pourbaix diagram of FeN_4C_{138}, HO-FeN_4C_{138}, and their dissolution states (Fe^{2+} and Fe^{3+}) at 298.15 K (right). Plots are reprinted with permission from ref. 165 and 166. (c) Comparison of Fe–N–C demetalation between Ar- and O_2-saturated alkaline (0.1 M NaOH) environments. The current density profile (top) and corresponding Fe dissolution rate and amount of dissolved Fe (bottom). The plot in (c) is adapted with permission from ref. 167. (d) Alkaline durability test results for the AEMFCs using FeCo–N–C (left) and Fe–N–C (right) are reprinted with permission from ref. 168 and 169, respectively.

ions, releasing OH• radicals. The OH• radical results in surface oxidation of the carbon of Fe–N–C, reducing the electrical conductivity, inducing demetalation due to structural collapse, and decreasing the TOF due to a change in the electrical structure. Under acidic conditions, the surface oxidation is significant because the OH• radical is stably maintained. In contrast, under alkaline conditions, the formation of the ferryl ion species (FeO^{2+}), which is less reactive with carbon, is more preferred over the OH• radical, resulting in higher stability of carbon compared to that under acidic conditions. In addition, the dissolved Fe^{2+} and Fe^{3+} are readily precipitated in their hydroxide forms ($Fe(OH)_2$ and $Fe(OH)_3$, respectively), preventing OH• radical formation. Holby *et al.* investigated the stability of a Fe–N–C catalyst through density functional theory (DFT) calculations.[166] As shown on the right side of Fig. 14b, the FeN_4C_{138} catalyst is stable in the pH range of 3–16, whereas Fe^{2+} dissolution could occur below pH 2 in an operating voltage range of OCV–0.4 V.

In contrast to the reports mentioned above, some studies have reported the degradation of Fe–N–C catalysts under alkaline environments. Recently, Ku *et al.* reported that a Fe–N–C catalyst can be dissolved due to the occurrence of ORR.[167] Comparison of Fe dissolution from the Fe–N–C catalyst between Ar- and O_2-saturated 0.1 M NaOH solution (Fig. 14c) shows that the dissolution rate is much faster in the presence of O_2. Another important feature is that Fe dissolution begins to occur as soon as the ORR current flows and that it is proportional to the current density. On the basis of these observations, they proposed that Fe dissolution is induced by the instability of the coordinated Fe during the Fe^{3+}/Fe^{2+} redox reaction during the course of the ORR. The instability of Fe–N–C was also observed under actual AEMFC operation. As shown in Fig. 14d (left), an AEMFC using the FeCo–N–C catalyst for the cathode CL showed a degradation rate of 1.7 mV h^{-1} at 0.6 A cm^{-2}.[168] Similarly, an AEMFC utilizing a silica-templated porous Fe–N–C catalyst exhibited a degradation rate of 0.46 mV h^{-1} during 150 h of 0.6 A cm^{-2} operation (Fig. 16d (right)).[16] Taken together, the electrochemical stabilities of Fe–N–C catalysts under alkaline conditions are still the subject of debate and the degradation pathways of Fe–N–C catalysts are not fully clear, highlighting the need for additional research.

5.2. AEMs and AEIs

5.2.1. Alkaline stabilities of AEMs. Recent progress in the development of long-lasting AEMFCs can be primarily attributed to advancements in the alkaline durability of AEMs and AEIs. The alkaline durability of these materials is dependent on their molecular structures as well as operating conditions, such as concentration of alkali, temperature, and humidity. Fig. 15a displays the retention of ionic conductivity after storage time in a 1 M alkaline solution for the recently reported AEMs. More detailed information on the AEM structure, test conditions, and

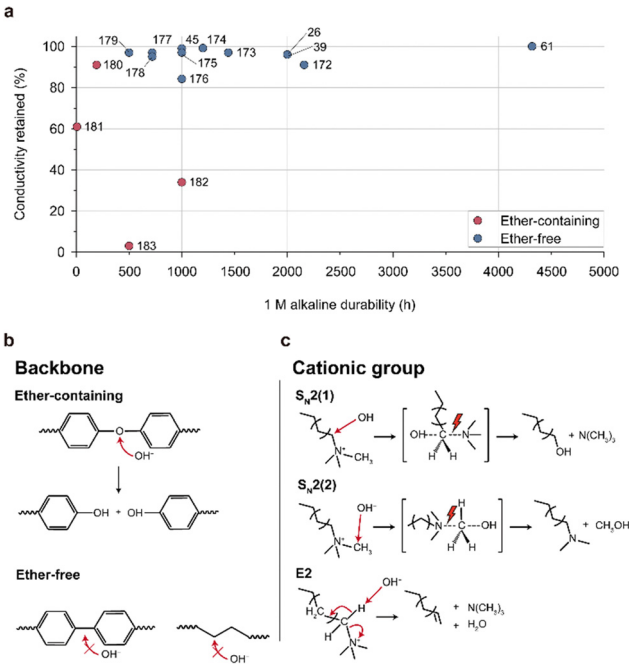

Fig. 15 Alkaline stability and degradation mechanism of the AEM. (a) Alkaline stability of ether-containing and ether-free AEMs in a 1 M alkaline solution (Table 8).[26,39,45,61,172–183] Alkaline degradation pathways for the (b) backbone structures (ether-containing and ether-free) and (c) cationic group (hexylTMA) in AEMs.

conductivity retention is presented in Table 8. Over the past few decades, most AEMs have been composed of an ether-containing backbone, particularly polyphenylene oxide, owing to its flexibility and ease of synthesis. However, these polymers lose their ionic conductivities over a short period of time under 1 M alkaline conditions (Fig. 15a) because the electron-deficient ether group is susceptible to nucleophilic OH^- attacks, causing it to break down into two hydroxyl groups (Fig. 15b).

In recent years, new-generation AEMs, which have an ether-free backbone such as polyphenylene and polyolefins, have been proposed and their enhanced alkaline stabilities have been reported. The delocalized electron densities of these ether-free AEMs enable them to endure nucleophilic OH^- attacks (Fig. 15b). Indeed, the ether-free AEMs demonstrate exceptional durability in 1 M alkaline solution (>1000 h operation while retaining >90% of their initial conductivities) (Fig. 15a). However, the use of an ether-free backbone does not completely prevent the decrease in ionic conductivity because of the degradation of the cationic groups that impart ionic conductivity. The alkaline degradation pathway for the representative cationic group, hexylTMA, is presented in Fig. 15c. The hexylTMA group is commonly degraded by nucleophilic substitution (S_N2) and Hofmann elimination (E2). In the S_N2 reaction, the OH^- molecule attacks the carbon atom linked to the nitrogen atom in the cationic group, forming the hydroxyl group. At this moment, the OH^- molecule can attack both the backbone side ($S_N2(1)$) and methyl side ($S_N2(2)$) carbons connected to the nitrogen atom; thus, the two pathways are possible. For the E2 reaction, the OH^- molecule attacks the hydrogen atom of the carbon from the hexyl group and forms H_2O; in this case, the C–H and C–N bonds break and the C=C double bond forms simultaneously.

To enable facile conduction of OH^-, the cationic groups in AEMs must be both positively charged and highly polarized. This polarization leads to the localization of electrons near the cation groups. As a result, the nucleophilic OH^- ion can attack the electron-deficient site, which can ultimately lead to decomposition of the cationic group. To address this issue, we suggest that the best cationic structures are those that are highly polarized with low pK_b values and that can also sterically hinder OH^- access to the electron-deficient sites. Additionally, incorporating a structure capable of minimizing the localization of electrons would also be preferable.

5.2.2. Alkaline stability of the AEI binder. Since the water is consumed at the cathode, the hydration level at the cathode decreases with operating time or current (Fig. 16a). Dekel *et al.* predicted a decrease in the hydration level at the cathode upon cell operation and a consequent exponential increase in the

Table 8 Chemical structures, alkaline stability test conditions, storage times, and ionic conductivity retentions after the alkaline stability test for AEIs displayed in Fig. 15a

AEM type	Chemical structure	Alkaline stability test condition	Test time (h)	Conductivity retention (%)	Ref.
Ether-free	Poly(vinylferrocene)	1 M NaOH, 95 °C	4320	100	61
	Poly(aryl-*co*-aryl piperidinium)	1 M KOH, 80 °C	2160	91	172
	Poly(aryl piperidinium)	1 M NaOH 100 °C	2000	96	26
	Poly(fluorenyl aryl piperidinium)	1 M NaOH 80 °C	2000	96	39
	Poly(terphenylene) with TMA	1 M KOH 95 °C	1440	98	173
	Poly(norbornene) with TMA	1 M KOH 80 °C	1200	99	174
	Poly(norbornene) with TMA	1 M NaOH 80 °C	1000	99	45
	Poly(fluoroalkylene-*co*-phenylene) with TMA	1 M KOH 80 °C	1000	97	175
	Poly(olefin) with TMA	1 M KOH 80 °C	1000	84	176
	Poly(fluorene) with TMA	1 M KOH 80 °C	720	97	177
	Poly(ethylene) with imidazolium	1 M KOH 80 °C	720	95	178
	Poly(fluoroalkylene-*co*-phenylene) with TMA	1 M KOH 80 °C	500	97	179
Ether-containing	Poly(phenylene oxide) with piperidium	1 M KOH 90 °C	192	91	180
	Poly(sulfone) with TMA	1 M KOH 50 °C	6	61	181
	Poly(arylene ether sulfone ketone-*co*-phenylene) with TMA	1 M KOH 60 °C	1000	34	182
	Partially fluorinated poly(arylene ether-*co*-phenylene) with TMA	1 M KOH 80 °C	500	3	183

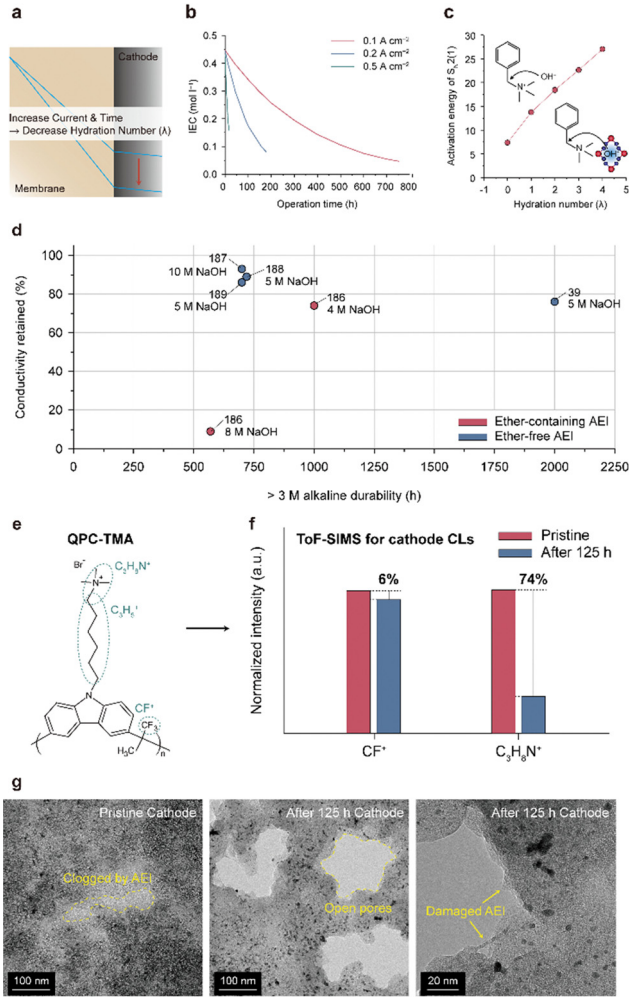

Fig. 16 Decomposition of the AEI at the cathode CL owing to the highly alkaline environment. (a) Changes in water concentrations at the cathode and membrane with operation time or current. (b) Predicted IEC of the AEI at the cathode during constant current operation at various current densities. (c) Correlation between the activation energy of $S_N2(1)$ reaction and hydration number of OH^-. Panels (b) and (c) are reprinted with permission from ref. 184 and 185, respectively. (d) Retention of ionic conductivity under storage in a highly concentrated alkaline solution for various AEIs (Table 9).[39,186–189] (e)–(g) Degradation of QPC-TMA ionomer in the cathode CL during constant current single-cell operation. (e) Chemical structure of the QPC-TMA. (f) ToF-SIMS intensities of CF^+ and $C_3H_8N^+$ and (g) TEM images of the cathode CL before and after 125 h of operation at 0.6 A cm^{-2}. Panels (e)–(g) are reprinted with permission from ref. 163.

degradation kinetic coefficient of trimethylbutylamine (TMBA) at the cathode based on a mathematical model.[184] They simulated the average IEC of the cathode AEI during constant current AEMFC operations at different current densities and found that the rate of IEC decrease increased with increasing operating current density (Fig. 16b). Furthermore, they demonstrated that the activation energy for $S_N2(1)$ degradation of the TMBA moiety decreased with the decreasing hydration level through *ex situ* experiments and DFT simulations (Fig. 16c),[185] indicating that $S_N2(1)$ degradation becomes more severe at lower hydration levels. Given the highly alkaline environment experienced during actual application of the AEI binders, the stability of the AEI in a highly concentrated alkaline solution may be more important than that in a 1 M alkaline solution. Fig. 16d displays the stabilities of ether-free AEIs in a highly concentrated alkaline solution (>3 M). Table 9 lists the structures, measurement conditions, and conductivity retentions for the AEIs compared in this figure. The alkaline stability in a highly concentrated alkali solution does not exceed 2000 h for the AEIs reported. In contrast to their high stability in 1 M KOH (Fig. 15a), the ether-free AEIs showed considerable loss in ionic conductivity in highly concentrated alkaline solutions owing to the degradation of the cationic groups. These findings suggest that when designing a cathode AEI, it is crucial to prioritize the alkaline resistance.

The deterioration of the cathode AEI during actual AEMFC operation was experimentally verified for a CL based on the QPC-TMA ionomer, whose structure is given in Fig. 16e. Hyun *et al.* investigated the relative amounts of the cationic group ($C_3H_8N^+$) and a main-chain moiety (CF^+) of the AEI in the cathode CL before and after 125 h of AEMFC operation at 0.6 A cm^{-2} using ToF-SIMS analysis.[163] As shown in Fig. 16f, the CF^+ intensity decreased by only 6%, whereas the $C_3H_8N^+$ intensity reduced by 74% after the operation, indicating significant degradation of the side-chain cationic group compared to the main chain. The TEM images of the cathode CL (Fig. 16g) demonstrate that the QPC-TMA phase, which clogs the interstitial pores between the Pt/C particles, was damaged after 125 h of cell operation, forming pores. In the high-magnification image, damaged QPC-TMA residues were identified at the perimeters of the pores.

In addition to chemical degradation under an alkaline environment, electrochemical reactions are another cause of AEI degradation at the cathode. Maurya *et al.* reported the electrochemical oxidations of phenyl-group-containing AEIs.[190] As shown in Fig. 17a, the cell voltage gradually decreased at a current density of 0.6 A cm^{-2} and 80 °C, followed by immediate recovery after alkaline solution replenishment by injection of 1 M KOH solution into the cell. The arrows in Fig. 17a indicate injection of the alkaline solution. The gain achieved through the replenishment process is regarded as a recoverable performance loss. However, despite the replenishment step, the initial cell voltage decreased gradually, as indicated by the dashed line, which is considered a permanent performance loss. The other interesting finding of this work is the decreased lifetime of the AEMFC with decreasing operating current (Fig. 17b), which implies that the cell durability is lower at higher cell voltages, which contrasts with the previous perception that the degradation of the cathode AEI becomes more severe with increasing operating current due to cathode dehydration.[184] The ^1H NMR analysis for the cathode AEI (BPN ionomer) before and after 75 h of operation at 0.9 V (Fig. 17c) shows that the phenylene moiety is oxidized and converted to phenol after operation. Based on these findings, they suggested that the permanent performance loss originates from phenyl oxidation (Fig. 17d). The phenyl groups of the AEI backbone adsorb onto the Pt surface and are electrochemically oxidized to phenol owing to the high potential at the ORR catalyst. The hydroxyl group of the phenol drags the TMA^+/OH^- pair and

Table 9 Chemical structures, alkaline stability test conditions, storage times, and ionic conductivity retention after alkaline stability tests for the AEIs displayed in Fig. 16d

Chemical structure	Alkaline stability test condition	Storage time (h)	Conductivity retention (%)	Ref.
Poly(fluorenyl aryl piperidinium)	5 M NaOH 80 °C	2000	76	39
Partially fluorinated poly(arylene ether-*co*-phenylene) with TMA	4 M KOH 80 °C	1000	74	186
Partially fluorinated poly(arylene ether-*co*-phenylene) with TMA	8 M KOH 80 °C	570	9	
Poly(olefin) with TMA	10 M NaOH 80 °C	700	93	187
Poly(aryl piperidinium)	5 M NaOH 80 °C	720	89	188
Quaternary ammonium-containing poly(olefins) with chain extenders	5 M NaOH 80 °C	700	87	189

reduces the pH at the ORR catalyst/AEI interface, resulting in decreased ORR kinetics in the AEMFC (Fig. 17e).

5.3. Mechanical durability of the AEMFC

In addition to chemical durability, mechanical durability is an essential factor for achieving long-lasting AEMFCs. In the PEMFC field, the mechanical durability of the membrane is a critical issue, and it is enhanced by either designing an ionomer structure or incorporating a reinforcing element, such as a porous support and filler. To assess the mechanical durability of CEMs, the essential work of fracture and tensile tests were suggested and demonstrated.[191] Considering the repeated volume expansion and shrinkage of the AEM during dynamic operation, mechanical failure of the AEM can include the formation of pinholes or cracks in the AEM and delamination between the AEM and CL (Fig. 18a). For PEMFC MEAs, CLs strongly bind with the membrane *via* thermal lamination as an external reinforcement; however, the thermal lamination method does not always work optimally with AEMs. The mechanical disintegration of the CLs can be an important degradation mode in AEMFCs; however, this issue has not been investigated yet.

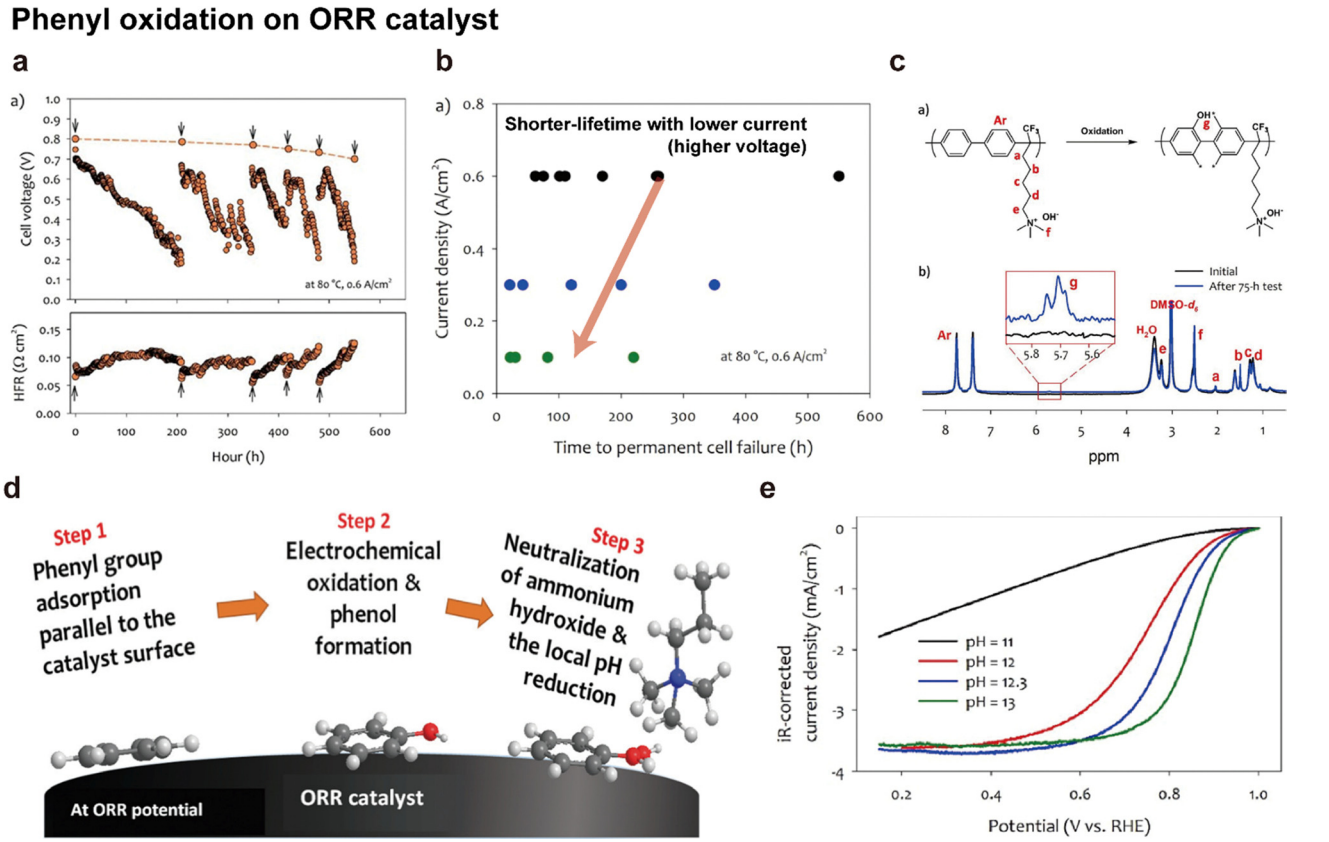

Fig. 17 Permanent performance degradation of AEMFCs caused by oxidation of the phenylene backbone of the AEI on ORR catalyst. (a) Cell voltage and high frequency resistance changes under operation at 0.6 A cm^{-2}. (b) Correlation between cell operating current density and time to permanent cell failure for an AEMFC MEA. The MEAs were constructed using *m*-TPN AEM, quaternized poly(fluorene) (FLN) AEI, and Pt/C for the cathodes and PtRu/C for the anode. (c) Structural changes in the quaternized poly(biphenylene) (BPN) ionomer due to phenyl oxidation on the cathode catalyst surface (top) and ^{1}H NMR spectra of the BPN ionomer before and after 75 h of holding test at 0.9 V. (d) Schematic illustration of the phenyl oxidation process on ORR catalyst. (e) ORR voltammograms of the Pt polycrystalline RDE in pH-controlled NaOH solutions. The rotating speed and scan rate were 1600 rpm and 20 mV s^{-1}, respectively. Panels (a)–(e) are adapted with permission from ref. 190 and 146, respectively.

The most commonly used durability test protocol for evaluating the mechanical stability of a fuel cell is wet/dry cycling that consists of repeating stages of fully humid and dry conditions every 2 min (Fig. 18b). Although originally developed for PEMFCs, the test can also be applied to AEMFCs. Fig. 18c shows the change in hydrogen cross-over with the wet/dry cycle number for an MEA with PiperION AEM[26] and one with a composite membrane consisting of a porous polyethylene membrane and the PDTP-RCM ionomer.[38] The reinforced membrane exhibited superior durability, and hydrogen cross-over barely occurred over 2000 wet/dry cycles.

Fig. 18d shows the changes in OCV and Ohmic resistance for MEAs using various AEMs (QPC-TMA, Sustainion, FAA-3, and PiperION) as functions of the wet/dry cycle number (our data that has not been published yet). Except for PiperION, all AEMs exhibited a drop in OCV below 0.9 V within 600 cycles. The significant decrease in the OCV implies that H_2 and O_2 gases pass through the AEMs owing to their mechanical damage. A post-mortem analysis (Fig. 18e) revealed membrane tearing at the edge of the CL for the QPC-TMA and Sustainion AEMs and pinholes for FAA-3. In contrast, the PiperION AEM did not show any notable membrane failure. Although the PiperION-based MEA maintained the initial OCV value, the Ohmic resistance abruptly rose after 1200 cycles, and the *i–V* power performance was significantly reduced after 1800 cycles, as shown in Fig. 18f. Such degradation can be caused by delamination of the AEM/CL interface or disintegration of the CL. The superior wet/dry cycling stability of PiperION can be attributed to its high ultimate stress compared with other AEMs (Fig. 18g).

Xu's group also reported interfacial delamination between the AEM and CL and used a thermally cross-linked AEM (CBBQPPO) (Fig. 18h) to achieve a robust interface.[192] For the reference membrane where a 3D-zipped structure is not applied, the interface was delaminated after AEMFC operation at 70 °C (Fig. 18i left). In contrast, when the thermally cross-linked AEM and AEI binder were used, the AEM/CL interface was stably maintained after AEMFC testing (Fig. 18i right). The strong AEM/CL interface resulting from the cross-linking enables over 120 h of operation at 0.6 A cm^{-2} while the other MEAs without 3D-zipped interfaces show rapid voltage losses.

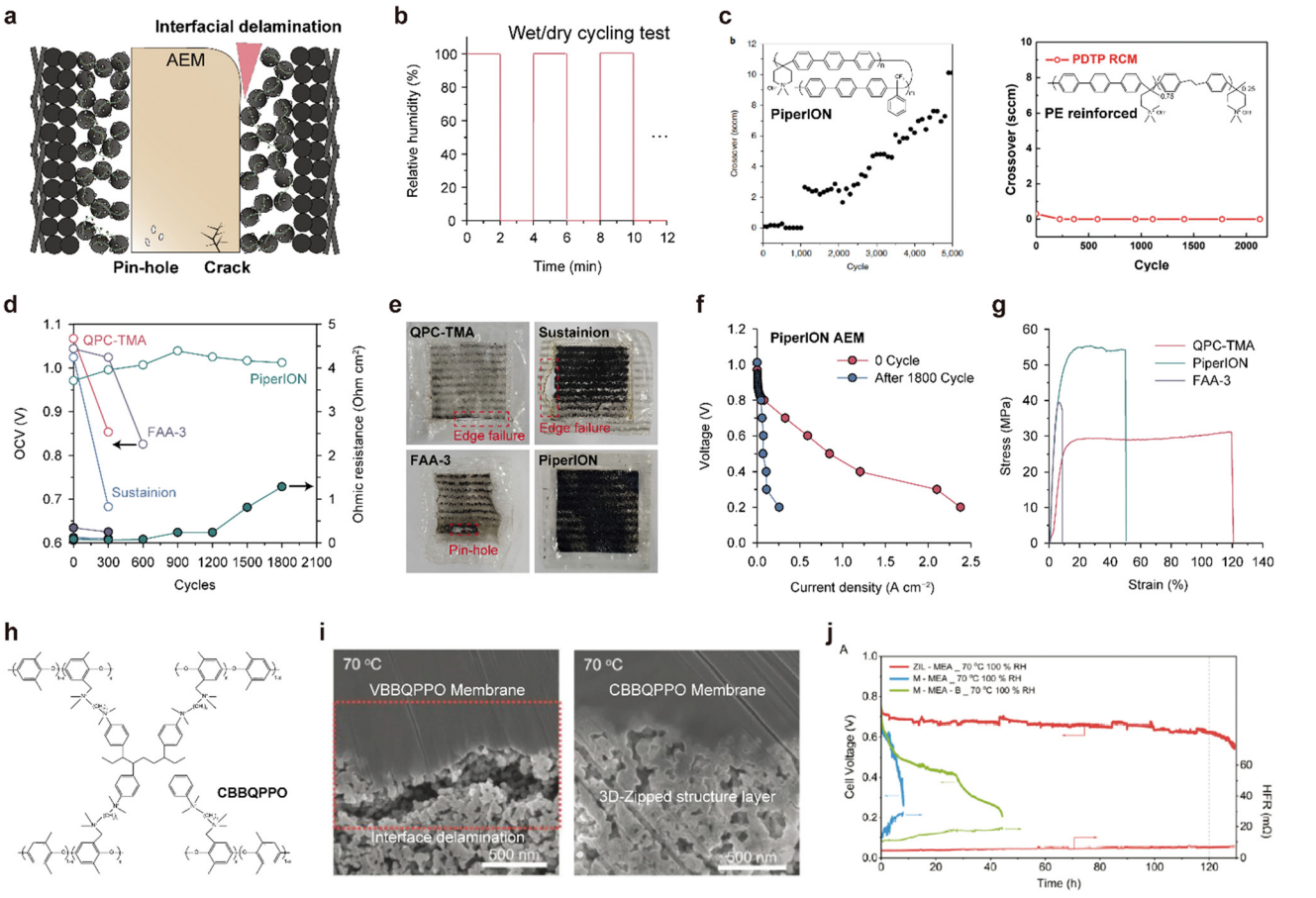

Fig. 18 Mechanical instability of the AEMFC MEA. (a) Mechanical deterioration modes for the AEMFC MEA. (b) Humidity changes under wet/dry cycling test. (c) Hydrogen cross-over changes with wet/dry cycling for the MEA using PipeION AEM (left) and a reinforced membrane (PDTP-RCM) with a porous polyethylene film (right). Data in (c) are adapted with permission from ref. 26 and 38. (d) Changes in OCV and Ohmic resistance with the wet/dry cycle number for the QPC-TMA, PiperION, FAA-3, and Sustainion AEMs. (e) Optical images of the membranes after wet/dry cycling tests. (f) *i–V* polarization curves of the MEA with the PiperION AEM before and after 1800 wet/dry cycles. (g) Stress–strain curves of QPC-TMA, PiperION, and FAA-3 AEMs. (h) Chemical structure of a 3D-zipped ionomer (CBBQPPO). (i) SEM images of the membrane/CL interface for the MEAs using the control (without 3D-zipped process, VBBQPPO) and 3D-zipped ionomers. (j) Voltage changes upon operation for the MEAs using the control (M-MEA and M-MEA-B) and 3D-zipped ionomers (ZIL-MEA). Data in (h)–(j) are reprinted with permission from ref. 192.

6. Outlook

Significant progress has been made in the development of AEMs and AEIs, thereby greatly improving the performances of AEMFCs. This has increased expectations for AEMFCs as viable alternatives to PEMFCs. However, from a commercialization perspective, AEMFCs still require substantial leaps forward in increasing their cost-competitiveness, durability, and reliability. Current AEMFC studies mainly deal with materials and MEAs; however, successful system development requires delicate water and thermal management, which is missing.

Although achieving higher power performance is desirable, it is essential to note that AEMFCs require significant amounts of Pt compared to PEMFCs. This negates the inherent incentive for cost-competitiveness. To address this issue, it is necessary to design a CL that maximize the ECSA or to develop catalysts with higher electrochemical activities. Mitigating the water imbalance is also necessary to augment the ECSA. Additionally, iterative MEA designs with lower amounts of Pt catalyst are required to identify factors that limit their performance. In the PEMFC technology sector, optimal CL structures have been designed by tuning the catalyst/ionomer compositions and their distribution. The remarkably high specific power density of PEMFCs (>8 W cm^{-2} $mg_{Pt}{}^{-1}$) resulting from long-term accumulated efforts in optimizing the CL structure can motivate further research on the CL designs of AEMFCs.

An intuitive way to increase the cost competitiveness of AEMFCs is to use non-Pt catalysts as the ORR catalysts as they have higher ORR activities in bases than acids. However, the design of a CL exploiting non-Pt catalysts presents a lot of challenges. Owing to the low volumetric density of electrochemically active sites, the CL thickness can be quite large at the catalyst loading level required for high power performance, resulting in large electrical resistances and/or mass transport resistances. The large and inhomogeneous sizes of the current non-Pt catalysts hinder the expansion of ionomer/catalyst contact. Therefore, more full-cell-level studies on cathode CLs based on non-Pt catalysts are needed.

Regarding the use of non-precious-metal catalysts for the anode, current HOR catalysts do not deliver high enough activities to replace Pt/C catalysts. Given the susceptibility of AEMFC anodes to water flooding, a physical structure that facilitates efficient drainage of water and gas diffusion must be considered in addition to the HOR activity. Carbon supports with hydrophobic surface modifications[143] or mesoporous structures (CNovel™ from Toyo Tanso)[193,194] can be good options. Additionally, the problem of strong adsorption of the AEI binder on the surface of the HOR catalyst should be addressed. The structural design of the AEI based on the calculation of the binding energy to the catalyst surface and tuning the AEI distribution in the CL can be effective approaches.

Durability is the biggest hurdle for AEMFCs from a practical standpoint, but it has not been fully emphasized in favor of presenting high power performances in a competitive manner. In sharp contrast to the durability of PEMFCs (over 10 000 h in a stack), AEMFCs have delivered a maximum of 2000 h of operation at the single-cell level. In our opinion, the most critical problem is the insufficient understanding of the key factors causing degradation during cell operation. To the best of our knowledge, the durability of AEMFCs has only been evaluated at constant current. However, considering the operating environments of real fuel cells, the current values are bound to vary depending on the power requirements. At this time, the water distribution of the MEA changes dynamically, and the degradation behavior also changes. Therefore, it is necessary to evaluate the durability of AEMFCs in an environment where the current or RH value changes, and it is also necessary to develop a standard protocol for this purpose.

Another overlooked aspect of durability is the mechanical deterioration of materials and components, which is more important in automotive applications. Crack and pinhole formation in membranes during repeated swelling/drying of the AEM and AEI at startup/shutdown can lead to sudden death. The interfacial delamination of the AEM/CL and disintegration of the CL can result in a drop in cell performance. However, in contrast to the chemical durability of AEMFCs, the mechanical durability has not been the subject of intensive investigations, probably owing to the use of the constant current mode in durability tests, which may not lead to significant mechanical degradation. A test protocol that reflects dynamic operation of AEMFCs would hence be necessary to motivate research on mechanical durability.

CO_2 poisoning presents a potential risk for fuel cell system development. Even though electrochemical CO_2 scrubbing systems appear promising, it is questionable whether the scrubbing system is durable enough because it shares a lot of degradation mechanisms with AEMFCs. The consumption of H_2 fuel in the scrubbing system results in a loss of fuel efficiency in the total AEMFC system. A techno-economic analysis would be needed to assess the cost-effectiveness of an AEMFC paired with a CO_2 remover. A new strategy to resolve the CO_2 poisoning problem in an efficient and cost-effective manner will have a great impact on AEMFC technology.

Acquiring fabrication technologies for the membranes, catalysts, CLs, and MEAs are important milestones for advancing AEMFC technology. For example, the state-of-the-art CLs for AEMFCs conventionally employ the spray-coating method, because it enables the use of small amounts of catalysts and ionomers. For PEMFCs, spray coating was used in the early stages of MEA research; however, current PEMFC CLs are manufactured mainly by slurry-casting methods, which are compatible with the roll-to-roll process. Very recently, our group presented a slurry cast CL for AEMFCs, initiating the research on CL manufacturing.[195] It is essential that the fabrication technology keeps pace with materials development to ensure the successful advancement of AEMFC technology.

Considering the fuel cells for transport applications significantly require low humidity and high-temperature operation to minimize the need for radiators and balance of plant, research focusing on such harsh operating conditions is highly meaningful. However, few studies reported low humidity and high-temperature operation of AEMFCs.[61,196] More research would be needed to explore the possibility of simplifying the system by enabling low-humidity or high-temperature operations.

In summary, AEMFCs have significant potential to power the hydrogen future owing to their high cost competitiveness. Current strides in material developments have encouraged the community to move forward. However, to make AEMFCs practical, the next step should be achieving sufficient durability, incorporating non-precious-metal catalysts, and improving reliability by addressing problems such as CO_2 poisoning and water imbalance.

Author contributions

Jonghyun Hyun: conceptualization, investigation, visualization, and writing – original draft; Hee-Tak Kim: supervision, funding acquisition, project administration, and writing – review and editing.

Conflicts of interest

There are no conflicts to declare.

Acknowledgements

This work was supported by the Agency for Defense Development by the Korean Government (UD2200061D), the Technology Innovation Program (20011712) funded by the Ministry of Trade, Industry and Energy (MOTIE, Korea), and the Korea Institute of Energy Technology Evaluation and Planning (KETEP) and the Ministry of Trade, Industry and Energy (MOTIE, Korea) of the Republic of Korea (No. 20223030040220).

References

1 K. Kodama, T. Nagai, A. Kuwaki, R. Jinnouchi and Y. Morimoto, *Nat. Nanotechnol.*, 2021, **16**, 140–147.
2 D. A. Cullen, K. C. Neyerlin, R. K. Ahluwalia, R. Mukundan, K. L. More, R. L. Borup, A. Z. Weber, D. J. Myers and A. Kusoglu, *Nat. Energy*, 2021, **6**, 462–474.
3 F. Bidault and P. H. Middleton, 4.07 - Alkaline fuel cells: Theory and application, *Comprehensive Renewable Energy*, Elsevier, 2012, pp. 179–202.
4 S. Noh, J. Y. Jeon, S. Adhikari, Y. S. Kim and C. Bae, *Accounts Chem. Res.*, 2019, **52**, 2745–2755.
5 W. H. Lee, Y. S. Kim and C. Bae, *ACS Macro Lett.*, 2015, **4**, 814–818.
6 N. Ul Hassan, M. Mandal, G. R. Huang, H. A. Firouzjaie, P. A. Kohl and W. E. Mustain, *Adv. Energy Mater.*, 2020, **10**, 2001986.
7 T. J. Omasta, A. M. Park, J. M. LaManna, Y. F. Zhang, X. Peng, L. Q. Wang, D. L. Jacobson, J. R. Varcoe, D. S. Hussey, B. S. Pivovar and W. E. Mustain, *Energy Environ. Sci.*, 2018, **11**, 551–558.
8 X. Peng, D. Kulkarni, Y. Huang, T. J. Omasta, B. Ng, Y. W. Zheng, L. Q. Wang, J. M. LaManna, D. S. Hussey, J. R. Varcoe, I. V. Zenyuk and W. E. Mustain, *Nat. Commun.*, 2020, **11**, 3561.
9 **https://www.londonstockexchange.com/**(accessed 13 April, 2023).
10 DOE Fundamentals Handbook, Chemistry, Volume 1 of 2.
11 M. Chatenet, S. Berthon-Fabry, Y. Ahmad, K. Guerin, M. Colin, H. Farhat, L. Frezet, G. Zhang and M. Dubois, *Adv. Energy Mater.*, 2023, **13**, 2204304.
12 L. Q. Wang, J. J. Brink, Y. Liu, A. M. Herring, J. Ponce-Gonzalez, D. K. Whelligan and J. R. Varcoe, *Energy Environ. Sci.*, 2017, **10**, 2154–2167.
13 L. Q. Wang, X. Peng, W. E. Mustain and J. R. Varcoe, *Energy Environ. Sci.*, 2019, **12**, 1575–1579.
14 M. Sharma, J. H. Jang, D. Y. Shin, J. A. Kwon, D. H. Lim, D. Choi, H. Sung, J. Jang, S. Y. Lee, K. Y. Lee, H. Y. Park, N. Jung and S. J. Yoo, *Energy Environ. Sci.*, 2019, **12**, 2200–2211.
15 R. Ren, C. Ge, Q. Li, G. Wang, L. Xiao, J. Lu and L. Zhuang, *J. Power Sources*, 2023, **556**, 232439.
16 H. Adabi, A. Shakouri, N. Ul Hassan, J. R. Varcoe, B. Zulevi, A. Serov, J. R. Regalbuto and W. E. Mustain, *Nat. Energy*, 2021, **6**, 834–843.
17 Y. R. Xue, L. Shi, X. R. Liu, J. J. Fang, X. D. Wang, B. P. Setzler, W. Zhu, Y. S. Yan and Z. B. Zhuang, *Nat. Commun.*, 2020, **11**, 5651.
18 Y. Wang, Y. Yang, S. F. Jia, X. M. Wang, K. J. Lyu, Y. Q. Peng, H. Zheng, X. Wei, H. Ren, L. Xiao, J. B. Wang, D. A. Muller, H. D. Abruna, B. O. E. Hwang, J. T. Lu and L. Zhuang, *Nat. Commun.*, 2019, **10**, 1506.
19 G. Meyer, C. Perrot, G. Gebel, L. Gonon, S. Morlat and J. L. Gardette, *Polymer*, 2006, **47**, 5003–5011.
20 C. Genies, R. Mercier, B. Sillion, R. Petiaud, N. Cornet, G. Gebel and M. Pineri, *Polymer*, 2001, **42**, 5097–5105.
21 K. Miyatake, H. Zhou, T. Matsuo, H. Uchida and M. Watanabe, *Macromolecules*, 2004, **37**, 4961–4966.
22 Y. Chikashige, Y. Chikyu, K. Miyatake and M. Watanabe, *Macromolecules*, 2005, **38**, 7121–7126.
23 S. J. Hong, H. Y. Jung, S. J. Yoon, K.-H. Oh, S.-G. Oh, Y. T. Hong, D. M. Yu and S. So, *J. Power Sources*, 2022, **551**, 232221.
24 D. P. Leonard, M. Lehmann, J. M. Klein, I. Matanovic, C. Fujimoto, T. Saito and Y. S. Kim, *Adv. Energy Mater.*, 2023, **13**, 2203488.
25 D. P. Leonard, S. Maurya, E. J. Park, L. D. Manriquez, S. Noh, X. F. Wang, C. Bae, E. D. Baca, C. Fujimoto and Y. S. Kim, *J. Mater. Chem. A*, 2020, **8**, 14135–14144.
26 J. H. Wang, Y. Zhao, B. P. Setzler, S. Rojas-Carbonell, C. Ben Yehuda, A. Amel, M. Page, L. Wang, K. Hu, L. Shi, S. Gottesfeld, B. J. Xu and Y. S. Yan, *Nat. Energy*, 2019, **4**, 392–398.
27 Y. Huang, Y. H. Pan, W. W. Wang, L. Jiang and Y. Dan, *Mater. Design*, 2019, **162**, 285–292.
28 M. H. Russell, W. R. Berti, B. Szostek and R. C. Buck, *Environ. Sci. Technol.*, 2008, **42**, 800–807.
29 S. Proch, M. Stenstrom, L. Eriksson, J. Andersson, G. Sjoblom, A. Jansson and J. Westlinder, *Int. J. Hydrogen Energy*, 2020, **45**, 1313–1324.
30 K. H. Cho, W. G. Lee, S. B. Lee and H. Jang, *J. Power Sources*, 2008, **178**, 671–676.

31 K. Feng, Y. Shen, J. M. Mai, D. A. Liu and X. Cai, *J. Power Sources*, 2008, **182**, 145–152.
32 Q. Zhang, S. Dong, P. Shao, Y. Zhu, Z. Mu, D. Sheng, T. Zhang, X. Jiang, R. Shao, Z. Ren, J. Xie, X. Feng and B. Wang, *Science*, 2022, **378**, 181–186.
33 Z. P. Zhao, Z. Y. Liu, A. Zhang, X. X. Yan, W. Xue, B. S. Peng, H. L. Xin, X. Q. Pan, X. F. Duan and Y. Huang, *Nat. Nanotechnol.*, 2022, **17**, 968–975.
34 Z. Y. Chen, C. Hao, B. W. Yan, Q. Y. Chen, H. Y. Feng, X. Q. Mao, J. M. Cen, Z. Q. Tian, P. Tsiakaras and P. K. Shen, *Adv. Energy Mater.*, 2022, **12**, 2201600.
35 A. Avid, J. L. Ochoa, Y. Huang, Y. C. Liu, P. Atanassov and I. V. Zenyuk, *Nat. Commun.*, 2022, **13**, 6349.
36 J. Hyun, J. Y. Jeon, G. Doo, J. Jung, S. Choi, D. H. Lee, D. W. Lee, J. Kwen, W. Jo, C. Bae and H. T. Kim, *Chem. Eng. J.*, 2022, **427**, 131737.
37 R. J. Gao, J. Wang, Z. F. Huang, R. R. Zhang, W. Wang, L. Pan, J. F. Zhang, W. K. Zhu, X. W. Zhang, C. X. Shi, J. Lim and J. J. Zou, *Nat. Energy*, 2021, **6**, 614–623.
38 C. Hu, J. H. Park, H. M. Kim, H. H. Wang, J. Y. Bae, M. L. Liu, N. Y. Kang, K. S. Yoon, C. D. Park, N. Chen and Y. M. Lee, *J. Mater. Chem. A*, 2022, **10**, 6587–6595.
39 N. J. Chen, H. H. Wang, S. P. Kim, H. M. Kim, W. H. Lee, C. Hu, J. Y. Bae, E. S. Sim, Y. C. Chung, J. H. Jang, S. J. Yoo, Y. B. Zhuang and Y. M. Lee, *Nat. Commun.*, 2021, **12**, 2367.
40 S. Maurya, S. Noh, I. Matanovic, E. J. Park, C. N. Villarrubia, U. Martinez, J. Han, C. Bae and Y. S. Kim, *Energy Environ. Sci.*, 2018, **11**, 3283–3291.
41 M. S. Cha, J. E. Park, S. Kim, S. H. Shin, S. H. Yang, S. J. Lee, T. H. Kim, D. M. Yu, S. So, K. M. Oh, Y. E. Sung, Y. H. Cho and J. Y. Lee, *J. Mater. Chem. A*, 2022, **10**, 9693–9706.
42 L. Zhu, X. Peng, S. L. Shang, M. T. Kwasny, T. J. Zimudzi, X. D. Yu, N. Saikia, J. Pan, Z. K. Liu, G. N. Tew, W. E. Mustain, M. Yandrasits and M. A. Hickner, *Adv. Funct. Mater.*, 2019, **29**, 1902059.
43 H. Cao, J. Pan, H. R. Zhu, Z. Sun, B. W. Wang, J. L. Zhao and F. Yan, *Adv. Sci.*, 2021, **8**, 2101744.
44 J. T. Fan, S. Willdorf-Cohen, E. M. Schibli, Z. Paula, W. Li, T. J. G. Skalski, A. T. Sergeenko, A. Hohenadel, B. J. Frisken, E. Magliocca, W. E. Mustain, C. E. Diesendruck, D. R. Dekel and S. Holdcroft, *Nat. Commun.*, 2019, **10**, 2306.
45 M. Mandal, G. Huang, N. Ul Hassan, W. E. Mustain and P. A. Kohl, *J. Mater. Chem. A*, 2020, **8**, 18386.
46 H. T. Chung, D. A. Cullen, D. Higgins, B. T. Sneed, E. F. Holby, K. L. More and P. Zelenay, *Science*, 2017, **357**, 479–483.
47 W. Wang, W. H. Chen, P. Y. Miao, J. Luo, Z. D. Wei and S. L. Chen, *ACS Catal.*, 2017, **7**, 6144–6149.
48 X. Wan, X. F. Liu, Y. C. Li, R. H. Yu, L. R. Zheng, W. S. Yan, H. Wang, M. Xu and J. L. Shui, *Nat. Catal.*, 2019, **2**, 259–268.
49 H. Zhang, H. T. Chung, D. A. Cullen, S. Wagner, U. I. Kramm, K. L. More, P. Zelenay and G. Wu, *Energy Environ. Sci.*, 2019, **12**, 2548–2558.
50 X. H. Xie, C. He, B. Y. Li, Y. H. He, D. A. Cullen, E. C. Wegener, A. J. Kropf, U. Martinez, Y. W. Cheng, M. H. Engelhard, M. E. Bowden, M. Song, T. Lemmon, X. S. Li, Z. M. Nie, J. Liu, D. J. Myers, P. Zelenay, G. F. Wang, G. Wu, V. Ramani and Y. Y. Shao, *Nat. Catal.*, 2020, **3**, 1044–1054.
51 L. Jiao, J. K. Li, L. L. Richard, Q. Sun, T. Stracensky, E. R. Liu, M. T. Sougrati, Z. P. Zhao, F. Yang, S. C. Zhong, H. Xu, S. Mukerjee, Y. Huang, D. A. Cullen, J. H. Park, M. Ferrandon, D. J. Myers, F. Jaouen and Q. Jia, *Nat. Mater.*, 2021, **20**, 1385–1391.
52 H. Xie, X. H. Xie, G. X. Hu, V. Prabhakaran, S. Saha, L. Gonzalez-Lopez, A. H. Phakatkar, M. Hong, M. L. Wu, R. Shahbazian-Yassar, V. Ramani, M. I. Al-Sheikhly, D. E. Jiang, Y. Y. Shao and L. B. Hu, *Nat. Energy*, 2022, **7**, 281–289.
53 J. Lilloja, E. Kibena-Poldsepp, A. Sarapuu, J. C. Douglin, M. Kaarik, J. Kozlova, P. Paiste, A. Kikas, J. Aruvali, J. Leis, V. Sammelselg, D. R. Dekel and K. Tammeveski, *ACS Catal.*, 2021, **11**, 1920–1931.
54 S. J. C. Cleghorn, D. K. Mayfield, D. A. Moore, J. C. Moore, G. Rusch, T. W. Sherman, N. T. Sisofo and U. Beuscher, *J. Power Sources*, 2006, **158**, 446–454.
55 R. Sharma, P. Morgen, S. Chiriaev, P. B. Lund, M. J. Larsen, B. Sieborg, L. Grahl-Madsen and S. M. Andersen, *ACS Appl. Mater. Inter.*, 2022, **14**, 49658–49671.
56 L. Dubau, L. Castanheira, M. Chatenet, F. Maillard, J. Dillet, G. Maranzana, S. Abbou, O. Lottin, G. De Moor, A. El Kaddouri, C. Bas, L. Flandin, E. Rossinot and N. Caque, *Int. J. Hydrogen Energy*, 2014, **39**, 21902–21914.
57 X. Cheng, L. Chen, C. Peng, Z. W. Chen, Y. Zhang and Q. B. Fan, *J. Electrochem. Soc.*, 2004, **151**, A48–A52.
58 A. Kannan, A. Kabza and J. Scholta, *J. Power Sources*, 2015, **277**, 312–316.
59 M. W. Fowler, R. F. Mann, J. C. Amphlett, B. A. Peppley and P. R. Roberge, *J. Power Sources*, 2002, **106**, 274–283.
60 K. H. Lee, D. H. Cho, Y. M. Kim, S. J. Moon, J. G. Seong, D. W. Shin, J. Y. Sohn, J. F. Kim and Y. M. Lee, *Energy Environ. Sci.*, 2017, **10**, 275–285.
61 X. Liu, N. Xie, J. D. Xue, M. Y. Li, C. Y. Zheng, J. F. Zhang, Y. Z. Qin, Y. Yin, D. R. Dekel and M. D. Guiver, *Nat. Energy*, 2022, **7**, 329–339.
62 H. Peng, Q. Li, M. Hu, L. Xiao, J. Lu and L. Zhuang, *J. Power Sources*, 2018, **390**, 165–167.
63 D. R. Dekel, *J. Power Sources*, 2018, **375**, 158–169.
64 A. Serov, I. V. Zenyuk, C. G. Arges and M. Chatenet, *J. Power Sources*, 2018, **375**, 149–157.
65 S. T. Thompson, D. Peterson, D. Ho and D. Papageorgopoulos, *J. Electrochem. Soc.*, 2020, **167**, 084514.
66 N. Ramaswamy and S. Mukerjee, *Adv. Phys. Chem.*, 2012, **2012**, 491604.
67 N. Ramaswamy and S. Mukerjee, *J. Phys. Chem. C*, 2011, **115**, 18015–18026.
68 J. Marcinkoski, *DOE Advanced Truck Technologies*, 2019, 1–31.
69 C. Y. Ahn, J. Ahn, S. Y. Kang, O. H. Kim, D. W. Lee, J. H. Lee, J. G. Shim, C. H. Lee, Y. H. Cho and Y. E. Sung, *Sci. Adv.*, 2020, **6**, eaaw0870.
70 X. Liu, Y. Li, J. D. Xue, W. K. Zhu, J. F. Zhang, Y. Yin, Y. Z. Qin, K. Jiao, Q. Du, B. W. Cheng, X. P. Zhuang, J. X. Li and M. D. Guiver, *Nat. Commun.*, 2019, **10**, 842.

71 C. S. Yin, J. J. Li, Y. W. Zhou, H. N. Zhan, P. F. Fang and C. Q. He, *ACS Appl. Mater. Inter.*, 2018, **10**, 14026–14035.
72 M. Mandal, G. Huang, N. Ul Hassan, W. E. Mustain and P. A. Kohl, *J. Mater. Chem. A*, 2020, **8**, 17568–17578.
73 J. S. Olsson, T. H. Pham and P. Jannasch, *Adv. Funct. Mater.*, 2018, **28**, 1702758.
74 X. L. Gao, L. X. Sun, H. Y. Wu, Z. Y. Zhu, N. Xiao, J. H. Chen, Q. Yang, Q. G. Zhang, A. M. Zhu and Q. L. Liu, *J. Mater. Chem. A*, 2020, **8**, 13065–13076.
75 J. Miyake, R. Taki, T. Mochizuki, R. Shimizu, R. Akiyama, M. Uchida and K. Miyatake, *Sci. Adv.*, 2017, **3**, eaao0476.
76 W. Jia, B. B. Tang and P. Y. Wu, *ACS Appl. Mater. Inter.*, 2017, **9**, 22620–22627.
77 Y. Kim, K. Ketpang, S. Jaritphun, J. S. Park and S. Shanmugam, *J. Mater. Chem. A*, 2015, **3**, 8148–8155.
78 Y. Sone, P. Ekdunge and D. Simonsson, *J. Electrochem. Soc.*, 1996, **143**, 1254–1259.
79 M. L. Wu, X. Zhang, Y. Zhao, C. P. Yang, S. S. Jing, Q. S. Wu, A. Brozena, J. T. Miller, N. J. Libretto, T. P. Wu, S. Bhattacharyya, M. N. Garaga, Y. G. Zhang, Y. Qi, S. G. Greenbaum, R. M. Briber, Y. S. Yan and L. B. Hu, *Nat. Nanotechnol.*, 2022, **17**, 629–636.
80 W. Yu, J. Zhang, X. Liang, X. L. Ge, C. P. Wei, Z. J. Ge, K. Y. Zhang, G. Li, W. J. Song, M. A. Shehzad, L. Wu and T. W. Xu, *J. Membr. Sci.*, 2021, **634**, 119404.
81 P. Atkins, P. W. Atkins and J. de Paula, *Atkins' physical chemistry*, Oxford University Press, 2014.
82 W. H. Lee, E. J. Park, J. Han, D. W. Shin, Y. S. Kim and C. Bae, *ACS Macro Lett.*, 2017, **6**, 566–570.
83 H. S. Dang and P. Jannasch, *J. Mater. Chem. A*, 2017, **5**, 21965–21978.
84 J. Pan, C. Chen, Y. Li, L. Wang, L. S. Tan, G. W. Li, X. Tang, L. Xiao, J. T. Lu and L. Zhuang, *Energy Environ. Sci.*, 2014, **7**, 354–360.
85 J. Pan, J. J. Han, L. Zhu and M. A. Hickner, *Chem. Mater.*, 2017, **29**, 5321–5330.
86 H. S. Dang and P. Jannasch, *Macromolecules*, 2015, **48**, 5742–5751.
87 L. Zhu, J. Pan, Y. Wang, J. J. Han, L. Zhuang and M. A. Hickner, *Macromolecules*, 2016, **49**, 815–824.
88 K. H. Lee, J. Y. Chu, A. R. Kim, H. G. Kim and D. J. Yoo, *J. Membr. Sci.*, 2021, **634**, 119435.
89 H. Chen, R. Tao, K. T. Bang, M. H. Shao and Y. Kim, *Adv. Energy Mater.*, 2022, **12**, 2200934.
90 N. Chen and Y. M. Lee, *Prog. Polym. Sci.*, 2021, **113**, 101345.
91 N. J. Chen and Y. M. Lee, *Trends Chem.*, 2022, **4**, 236–249.
92 A. Chakraborty, I. Salam, M. Choolaei, J. Lee, C. Crean, D. K. Whelligan, R. Bance-Soualhi and J. R. Varcoe, *Mater. Adv.*, 2023, **4**, 2099–2105.
93 S. Willdorf-Cohen, A. Zhegur-Khais, J. Ponce-Gonzalez, S. Bsoul-Haj, J. R. Varcoe, C. E. Diesendruck and D. R. Dekel, *ACS Appl. Energy Mater.*, 2023, **6**, 1085–1092.
94 S. Haj-Bsoul, J. R. Varcoe and D. R. Dekel, *J. Electroanal. Chem.*, 2022, **908**, 116112.
95 G. Huang, M. Mandal, X. Peng, A. C. Yang-Neyerlin, B. S. Pivovar, W. E. Mustain and P. A. Kohl, *J. Electrochem. Soc.*, 2019, **166**, F637–F644.
96 M. Lehmann, D. Leonard, J. C. Zheng, L. L. He, X. M. Tang, X. C. Chen, K. H. Lim, S. Maurya, Y. S. Kim and T. Saito, *ACS Appl. Energy Mater.*, 2023, **6**, 1822–1833.
97 M. Mandal, G. Huang, N. Ul Hassan, X. Peng, T. L. Gu, A. H. Brooks-Starks, B. Bahar, W. E. Mustain and P. A. Kohl, *J. Electrochem. Soc.*, 2019, **167**, 054501.
98 K. A. Mauritz and R. B. Moore, *Chem. Rev.*, 2004, **104**, 4535–4585.
99 D. W. Shin, M. D. Guiver and Y. M. Lee, *Chem. Rev.*, 2017, **117**, 4759–4805.
100 J. Hyun, G. Doo, S. Yuk, D. H. Lee, D. W. Lee, S. Choi, J. Kwen, H. Kang, R. Tenne, S. G. Lee and H. T. Kim, *ACS Appl. Energy Mater.*, 2020, **3**, 4619–4628.
101 P. Q. Yin, T. Yao, Y. Wu, L. R. Zheng, Y. Lin, W. Liu, H. X. Ju, J. F. Zhu, X. Hong, Z. X. Deng, G. Zhou, S. Q. Wei and Y. D. Li, *Angew. Chem., Int. Ed.*, 2016, **55**, 10800–10805.
102 W. J. Jiang, L. Gu, L. Li, Y. Zhang, X. Zhang, L. J. Zhang, J. Q. Wang, J. S. Hu, Z. D. Wei and L. J. Wan, *J. Am. Chem. Soc.*, 2016, **138**, 3570–3578.
103 D. N. Wang, Y. L. Wu, Z. G. Li, H. Pan, Y. Q. Wang, M. S. Yang and G. X. Zhang, *Chem. Eng. J.*, 2021, **424**, 130401.
104 Y. H. Han, Y. G. Wang, R. R. Xu, W. X. Chen, L. R. Zheng, A. J. Han, Y. Q. Zhu, J. Zhang, H. B. Zhang, J. Luo, C. Chen, Q. Peng, D. S. Wang and Y. D. Li, *Energy Environ. Sci.*, 2018, **11**, 2348–2352.
105 J. Guo, S. Gadipelli, Y. C. Yang, Z. N. Li, Y. Lu, D. J. L. Brett and Z. X. Guo, *J. Mater. Chem. A*, 2019, **7**, 3544–3551.
106 X. Peng, T. J. Omasta, E. Magliocca, L. Q. Wang, J. R. Varcoe and W. E. Mustain, *Angew. Chem., Int. Ed.*, 2019, **58**, 1046–1051.
107 H. Yin, C. Z. Zhang, F. Liu and Y. L. Hou, *Adv. Funct. Mater.*, 2014, **24**, 2930–2937.
108 Y. Yang, Y. Xiong, M. E. Holtz, X. Feng, R. Zeng, G. Chen, F. J. DiSalvo, D. A. Muller and H. D. Abruña, *Proc. Natl. Acad. Sci. U. S. A.*, 2019, **116**, 24425–24432.
109 R. Zeng, Y. Yang, X. Feng, H. Li, L. M. Gibbs, F. J. DiSalvo and H. D. Abruña, *Sci. Adv.*, 2022, **8**, eabj1584.
110 Y. Yang, R. Zeng, Y. Xiong, F. J. DiSalvo and H. D. Abruna, *Chem. Mater.*, 2019, **31**, 9331–9337.
111 F. Cheng, Y. Su, J. Liang, Z. Tao and J. Chen, *Chem. Mater.*, 2010, **22**, 898–905.
112 S. Kosasang, N. Ma, P. Wuamprakhon, N. Phattharasupakun, T. Maihom, J. Limtrakul and M. Sawangphruk, *Chem. Commun.*, 2018, **54**, 8575–8578.
113 X. Zhong, M. Oubla, X. Wang, Y. Huang, H. Zeng, S. Wang, K. Liu, J. Zhou, L. He, H. Zhong, N. Alonso-Vante, C.-W. Wang, W.-B. Wu, H.-J. Lin, C.-T. Chen, Z. Hu, Y. Huang and J. Ma, *Nat. Commun.*, 2021, **12**, 3136.
114 F. Moureaux, P. Stevens and M. Chatenet, *Electrocatalysis*, 2013, **4**, 123–133.
115 J. Vondrák, B. Klápště, J. Velická, M. Sedlaříková, J. Reiter, I. Roche, E. Chainet, J. F. Fauvarque and M. Chatenet, *J. New Mater. Electrochem. Syst.*, 2005, **8**, 209–212.
116 A. C. Garcia, J. J. Linares, M. Chatenet and E. A. Ticianelli, *Electrocatalysis*, 2014, **5**, 41–49.

117 I. Roche, E. ChaÎnet, M. Chatenet and J. Vondrák, *J. Phys. Chem. C*, 2007, **111**, 1434–1443.
118 F. D. Speck, P. G. Santori, F. Jaouen and S. Cherevko, *J. Phys. Chem. C*, 2019, **123**, 25267–25277.
119 T. Lazaridis, B. M. Stuhmeier, H. A. Gasteiger and H. A. El-Sayed, *Nat. Catal.*, 2022, **5**, 363–373.
120 R. Riasse, C. Lafforgue, F. Vandenberghe, F. Micoud, A. Morin, M. Arenz, J. Durst and M. Chatenet, *J. Power Sources*, 2023, **556**, 232491.
121 M. M. Hossen, M. S. Hasan, M. R. I. Sardar, J. bin Haider, Mottakin, K. Tammeveski and P. Atanassov, *Appl. Catal., B*, 2023, **325**, 121733.
122 N. Bevilacqua, T. Asset, M. A. Schmid, H. Markotter, I. Manke, P. Atanassov and R. Zeis, *J. Power Source Adv.*, 2021, **7**, 100042.
123 J. Durst, A. Siebel, C. Simon, F. Hasche, J. Herranz and H. A. Gasteiger, *Energy Environ. Sci.*, 2014, **7**, 2255–2260.
124 W. C. Sheng, Z. B. Zhuang, M. R. Gao, J. Zheng, J. G. G. Chen and Y. S. Yan, *Nat. Commun.*, 2015, **6**, 5848.
125 D. Strmcnik, M. Uchimura, C. Wang, R. Subbaraman, N. Danilovic, D. van der Vliet, A. P. Paulikas, V. R. Stamenkovic and N. M. Markovic, *Nat. Chem.*, 2013, **5**, 300–306.
126 J. H. Dumont, A. J. Spears, R. P. Hjelm, M. Hawley, S. Maurya, D. G. Li, G. C. Yuan, E. B. Watkins and Y. S. Kim, *ACS Appl. Mater. Inter.*, 2020, **12**, 1825–1831.
127 R. Sgarbi, H. Doan, V. Martin and M. Chatenet, *Electrocatalysis*, 2023, **14**, 267–278.
128 A. G. Oshchepkov, A. Bonnefont, V. N. Parmon and E. R. Savinova, *Electrochim. Acta*, 2018, **269**, 111–118.
129 A. G. Oshchepkov, G. Braesch, A. Bonnefont, E. R. Savinova and M. Chatenet, *ACS Catal.*, 2020, **10**, 7043–7068.
130 H. Doan, I. Kendrick, R. Blanchard, Q. Jia, E. Knecht, A. Freeman, T. Jankins, M. K. Bates and S. Mukerjee, *J. Electrochem. Soc.*, 2021, **168**, 084501.
131 H. Wang and H. D. Abruña, *J. Am. Chem. Soc.*, 2017, **139**, 6807–6810.
132 J. Zheng, Z. B. Zhuang, B. J. Xu and Y. S. Yan, *ACS Catal.*, 2015, **5**, 4449–4455.
133 J. Ohyama, T. Sato, Y. Yamamoto, S. Arai and A. Satsuma, *J. Am. Chem. Soc.*, 2013, **135**, 8016–8021.
134 W. Y. Ni, T. Wang, P. A. Schouwink, Y. C. Chuang, H. M. Chen and X. L. Hu, *Angew. Chem., Int. Ed.*, 2020, **59**, 10797–10801.
135 W. Y. Ni, A. Krammer, C. S. Hsu, H. M. Chen, A. Schuler and X. L. Hu, *Angew. Chem., Int. Ed.*, 2019, **58**, 7445–7449.
136 J. Wang, X. Dong, J. Liu, W. Z. Li, L. T. Roling, J. P. Xiao and L. H. Jiang, *ACS Catal.*, 2021, **11**, 7422–7428.
137 F. L. Yang, X. Bao, Y. M. Zhao, X. W. Wang, G. Z. Cheng and W. Luo, *J. Mater. Chem. A*, 2019, **7**, 10936–10941.
138 Z. B. Zhuang, S. A. Giles, J. Zheng, G. R. Jenness, S. Caratzoulas, D. G. Vlachos and Y. S. Yan, *Nat. Commun.*, 2016, **7**, 10141.
139 L. J. Gao, Y. Wang, H. B. Li, Q. H. Li, N. Ta, L. Zhuang, Q. Fu and X. H. Bao, *Chem. Sci.*, 2017, **8**, 5728–5734.
140 O. V. Cherstiouk, P. A. Simonov, A. G. Oshchepkov, V. I. Zaikovskii, T. Y. Kardash, A. Bonnefont, V. N. Parmon and E. R. Savinova, *J. Electroanal. Chem.*, 2016, **783**, 146–151.
141 I. Matanovic and Y. S. Kim, *Curr. Opin. Electrochem.*, 2023, **38**, 101218.
142 D. Choi, J. H. Jang, D. W. Lee, Y. S. Kang, H. Jin, K. Y. Lee and S. J. Yoo, *J. Power Sources*, 2021, **494**, 229738.
143 J. Hyun, W. Jo, S. H. Yang, S. H. Shin, G. Doo, S. Choi, D. H. Lee, D. W. Lee, E. Oh, J. Y. Lee and H. T. Kim, *J. Power Sources*, 2022, **543**, 231835.
144 G. Camera-Roda, A. Cardillo, V. Loddo, L. Palmisano and F. Parrino, *Membranes*, 2014, **4**, 96–112.
145 J. Zhang, Y. Liu, W. Zhu, Y. Pei, Y. Yin, Y. Qin, X. Li and M. D. Guiver, *Cell Rep. Phys. Sci.*, 2021, **2**, 100377.
146 W. E. Mustain, M. Chatenet, M. Page and Y. S. Kim, *Energy Environ. Sci.*, 2020, **13**, 2805–2838.
147 N. Ziv, A. N. Mondal, T. Weissbach, S. Holdcroft and D. R. Dekel, *J. Membr. Sci.*, 2019, **586**, 140–150.
148 Y. W. Zheng, T. J. Omasta, X. Peng, L. Q. Wang, J. R. Varcoe, B. S. Pivovar and W. E. Mustain, *Energy Environ. Sci.*, 2019, **12**, 2806–2819.
149 Y. W. Zheng, G. Huang, L. Q. Wang, J. R. Varcoe, P. A. Kohl and W. E. Mustain, *J. Power Sources*, 2020, **467**, 228350.
150 Y. W. Zheng, G. R. Huang, M. Mandal, J. R. Varcoe, P. A. Kohl and W. E. Mustain, *J. Electrochem. Soc.*, 2021, **168**, 024504.
151 L. Shi, Y. Zhao, S. Matz, S. Gottesfeld, B. P. Setzler and Y. S. Yan, *Nat. Energy*, 2022, **7**, 238–247.
152 G. Pellegrini, R. Strube and G. Manfrida, *Energy*, 2010, **35**, 851–857.
153 S. E. Renfrew, D. E. Starr and P. Strasser, *ACS Catal.*, 2020, **10**, 13058–13074.
154 T. Wang, L. Shi, J. Wang, Y. Zhao, B. P. Setzler, S. Rojas-Carbonell and Y. Yan, *J. Electrochem. Soc.*, 2019, **166**, F3305–F3310.
155 Z. Liang, F. Yang, Y. Li, J. Tang, D. R. Dekel and X. He, *Sep. Purif. Technol.*, 2022, **289**, 120713.
156 J. Zhang, W. Zhu, T. Huang, C. Zheng, Y. Pei, G. Shen, Z. Nie, D. Xiao, Y. Yin and M. D. Guiver, *Adv. Sci.*, 2021, **8**, 2100284.
157 Y. Yang, C. R. Peltier, R. Zeng, R. Schimmenti, Q. Li, X. Huang, Z. Yan, G. Potsi, R. Selhorst, X. Lu, W. Xu, M. Tader, A. V. Soudackov, H. Zhang, M. Krumov, E. Murray, P. Xu, J. Hitt, L. Xu, H.-Y. Ko, B. G. Ernst, C. Bundschu, A. Luo, D. Markovich, M. Hu, C. He, H. Wang, J. Fang, R. A. DiStasio, L. F. Kourkoutis, A. Singer, K. J. T. Noonan, L. Xiao, L. Zhuang, B. S. Pivovar, P. Zelenay, E. Herrero, J. M. Feliu, J. Suntivich, E. P. Giannelis, S. Hammes-Schiffer, T. Arias, M. Mavrikakis, T. E. Mallouk, J. D. Brock, D. A. Muller, F. J. DiSalvo, G. W. Coates and H. D. Abruna, *Chem. Rev.*, 2022, **122**, 6117–6321.
158 A. Carlson, P. Shapturenka, B. Eriksson, G. Lindbergh, C. Lagergren and R. W. Lindstrom, *Electrochim. Acta*, 2018, **277**, 151–160.
159 L. Tang, X. Li, R. C. Cammarata, C. Friesen and K. Sieradzki, *J. Am. Chem. Soc.*, 2010, **132**, 11722–11726.

160 A. Zadick, L. Dubau, N. Sergent, G. Berthome and M. Chatenet, *ACS Catal.*, 2015, **5**, 4819–4824.
161 C. Lafforgue, A. Zadick, L. Dubau, F. Maillard and M. Chatenet, *Fuel Cells*, 2018, **18**, 229–238.
162 C. Lafforgue, M. Chatenet, L. Dubau and D. R. Dekel, *ACS Catal.*, 2018, **8**, 1278–1286.
163 J. Hyun, S. H. Yang, G. Doo, S. Choi, D. H. Lee, D. W. Lee, J. Kwen, W. Jo, S. H. Shin, J. Y. Lee and H. T. Kim, *J. Mater. Chem. A*, 2021, **9**, 18546–18556.
164 C. Lafforgue, F. Maillard, V. Martin, L. Dubau and M. Chatenet, *ACS Catal.*, 2019, **9**, 5613–5622.
165 G. Bae, M. W. Chung, S. G. Ji, F. Jaouen and C. H. Choi, *ACS Catal.*, 2020, **10**, 8485–8495.
166 E. F. Holby, G. F. Wang and P. Zelenay, *ACS Catal.*, 2020, **10**, 14527–14539.
167 Y. P. Ku, K. Ehelebe, A. Hutzler, M. Bierling, T. Bohm, A. Zitolo, M. Vorokhta, N. Bibent, F. D. Speck, D. Seeberger, I. Khalakhan, K. J. J. Mayrhofer, S. Thiele, F. Jaouen and S. Cherevko, *J. Am. Chem. Soc.*, 2022, **144**, 9753–9763.
168 K. Kisand, A. Sarapuu, J. C. Douglin, A. Kikas, A. Treshchalov, M. Kaeaerik, H. M. Piirsoo, P. Paiste, J. Aruvaeli, J. Leis, V. Kisand, A. Tamm, D. R. Dekel and K. Tammeveski, *ACS Catal.*, 2022, **12**, 14050–14061.
169 C. H. Choi, H. K. Lim, M. W. Chung, G. Chon, N. R. Sahraie, A. Altin, M. T. Sougrati, L. Stievano, H. S. Oh, E. S. Park, F. Luo, P. Strasser, G. Drazic, K. J. J. Mayrhofer, H. Kim and F. Jaouen, *Energy Environ. Sci.*, 2018, **11**, 3176–3182.
170 K. Kumar, L. Dubau, M. Mermoux, J. K. Li, A. Zitolo, J. Nelayah, F. Jaouen and F. Maillard, *Angew. Chem., Int. Ed.*, 2020, **59**, 3235–3243.
171 P. G. Santori, F. D. Speck, J. Li, A. Zitolo, Q. Y. Jia, S. Mukerjee, S. Cherevko and F. Jaouen, *J. Electrochem. Soc.*, 2019, **166**, F3311.
172 N. Chen, C. Hu, H. H. Wang, J. H. Park, H. M. Kim and Y. M. Lee, *J. Membr. Sci.*, 2021, **638**, 119685.
173 E. J. Park, C. B. Capuano, K. E. Ayers and C. Bae, *J. Power Sources*, 2018, **375**, 367–372.
174 M. Mandal, G. Huang and P. A. Kohl, *J. Membr. Sci.*, 2019, **570**, 394–402.
175 H. Ono, T. Kimura, A. Takano, K. Asazawa, J. Miyake, J. Inukai and K. Miyatake, *J. Mater. Chem. A*, 2017, **5**, 24804–24812.
176 L. Zhu, X. D. Yu, X. Peng, T. J. Zimudzi, N. Saikia, M. T. Kwasny, S. F. Song, D. I. Kushner, Z. S. Fu, G. N. Tew, W. E. Mustain, M. A. Yandrasits and M. A. Hickner, *Macromolecules*, 2019, **52**, 4030–4041.
177 W. H. Lee, A. D. Mohanty and C. Bae, *ACS Macro Lett.*, 2015, **4**, 453–457.
178 W. You, E. Padgett, S. N. MacMillan, D. A. Muller and G. W. Coates, *Proc. Natl. Acad. Sci. U. S. A.*, 2019, **116**, 9729–9734.
179 A. M. A. Mahmoud, A. M. M. Elsaghier, K. Otsuji and K. Miyatake, *Macromolecules*, 2017, **50**, 4256–4266.
180 H. S. Dang and P. Jannasch, *J. Mater. Chem. A*, 2016, **4**, 11924–11938.
181 A. D. Mohanty, Y. B. Lee, L. Zhu, M. A. Hickner and C. Bae, *Macromolecules*, 2014, **47**, 1973–1980.
182 R. Akiyama, N. Yokota, E. Nishino, K. Asazawa and K. Miyatake, *Macromolecules*, 2016, **49**, 4480–4489.
183 N. Yokota, M. Shimada, H. Ono, R. Akiyama, E. Nishino, K. Asazawa, J. Miyake, M. Watanabe and K. Miyatake, *Macromolecules*, 2014, **47**, 8238–8246.
184 D. R. Dekel, I. G. Rasin and S. Brandon, *J. Power Sources*, 2019, **420**, 118–123.
185 D. R. Dekel, M. Arnar, S. Willdorf, M. Kosa, S. Dhara and C. E. Diesendruck, *Chem. Mater.*, 2017, **29**, 4425–4431.
186 A. M. A. Mahmoud and K. Miyatake, *J. Mater. Chem. A*, 2018, **6**, 14400–14409.
187 M. Zhang, C. R. Shan, L. Liu, J. Y. Liao, Q. Chen, M. Zhu, Y. G. Wang, L. A. An and N. W. Li, *ACS Appl. Mater. Inter.*, 2016, **8**, 23321–23330.
188 X. M. Du, H. Y. Zhang, Y. J. Yuan and Z. Wang, *J. Power Sources*, 2021, **487**, 229429.
189 M. Zhang, J. L. Liu, Y. G. Wang, L. A. An, M. D. Guiver and N. W. Li, *J. Mater. Chem. A*, 2015, **3**, 12284–12296.
190 S. Maurya, A. S. Lee, D. G. Li, E. J. Park, D. P. Leonard, S. Noh, C. Bae and Y. S. Kim, *J. Power Sources*, 2019, **436**, 226866.
191 E. Moukheiber, C. Bas and L. Flandin, *Int. J. Hydrogen Energy*, 2014, **39**, 2717–2723.
192 X. Liang, X. L. Ge, Y. B. He, M. Xu, M. A. Shehzad, F. M. Sheng, R. Bance-Soualhi, J. J. Zhang, W. S. Yu, Z. J. Ge, C. P. Wei, W. J. Song, J. L. Peng, J. R. Varcoe, L. Wu and T. W. Xu, *Adv. Sci.*, 2021, **8**, 2102637.
193 Y. J. Lee, H. E. Kim, E. Lee, J. Lee, S. Shin, H. Yun, E. J. Kim, H. Jung, H. C. Ham, B. J. Kim and H. Lee, *Adv. Energy Mater.*, 2021, **11**, 2102970.
194 Y. J. Lee, H. E. Kim, H. Oh, H. Yun, J. Lee, S. Shin, H. Lee and B. J. Kim, *ACS Nano*, 2022, **16**, 2988–2996.
195 J. Hyun, D. W. Lee, E. Oh, H. Bae, J. Park, G. Doo and H.-T. Kim, *J. Power Sources*, 2023, **573**, 233161.
196 J. C. Douglin, J. R. Varcoe and D. R. Dekel, *J. Power Sources Adv.*, 2020, **5**, 100023.

